

Rain Impacts on the Surface Atmosphere and Upper Ocean in the Central Equatorial Pacific

DANIEL B. WHITT^a

^a NASA Ames Research Center, Moffett Field, California

(Manuscript received 28 January 2022, in final form 7 May 2022)

ABSTRACT: The impacts of rainy days (>24 mm) on the physics of the surface atmosphere and upper ocean are characterized in the central Pacific Ocean (140° – 170° W) on the equator, where deep-cycle turbulence substantially influences the sea surface temperature and air–sea heat flux on diurnal and longer time scales. Here, rainfall is relatively weak on average (1 – 3 mm day $^{-1}$), and enough rain to substantially alter the diurnal cycle of upper-ocean buoyancy only occurs on the order of once in 100 days, albeit more frequently to the west and during El Niño and boreal winter. Rainy days are associated with multiple systematic changes in the surface atmosphere, but the freshwater and the reduction in daily downwelling shortwave radiation (by ~ 50 W m $^{-2}$) are codominant and drive systematic changes in the ocean during and the day after the rainy day. These two drivers explain ensemble average reductions in the upper-ocean salinity (-0.12 psu at 1 m) and temperature (-0.16° C at 1 m) and increases in buoyancy ($+0.0005$ m s $^{-2}$ at 1 m), which are typically confined to a shallow fresh/warm mixing layer on the order of 10 m thick in the daytime. At deeper depths, the intrinsic ocean temperature, salinity, and velocity variability make it challenging to extract an ensemble average response to rainy days in observations, but some examples from observations and large-eddy simulations suggest that rainfall can significantly reduce the vertical extent and heat flux in the deep-cycle turbulence, although the bulk energetics and buoyancy flux of the turbulence are not necessarily modified by rain.

SIGNIFICANCE STATEMENT: Rain significantly impacts social and ecological systems in many ways that are readily apparent in populated areas, but the impacts of rain over the ocean are not as well known. In this paper, sustained in situ observations over decades and highly resolved numerical simulations of ocean turbulence during a few rain events are used to characterize the impacts of rainy days on the surface–atmosphere and upper-ocean physics in the center of action of El Niño in the central equatorial Pacific. These results contribute to broader efforts to observe, understand, and accurately model the surface atmosphere, the upper ocean, and air–sea interaction in the central Pacific and thereby improve long-range weather and climate observations and predictions.


KEYWORDS: Atmosphere-ocean interaction; Mixing; Oceanic mixed layer; Rainfall; Large eddy simulations

1. Introduction

Rainwater is essentially salt-free and thus about 2% less dense than seawater. Rain therefore modifies the physics of the ocean surface boundary layer by changing the buoyancy. For example, studies have shown that rain is associated with changes in the evolution and vertical structure of the boundary layer salinity, temperature, and buoyancy (Price 1979; Anderson and Riser 2014; Asher et al. 2014; Drushka et al. 2016, 2019; Thompson et al. 2019), as well as momentum, kinetic energy, and turbulence (Price 1979; Anderson et al. 1996; Shcherbina et al. 2019; Clayson et al. 2019; ten Doeschate et al. 2019; Smyth et al. 1997; Wijesekera and Gregg 1996; Wijesekera et al. 1999; Iyer and Drushka 2021b,a). In addition, rain may deposit, dilute, or otherwise modify the concentration and air–sea exchange of biogeochemical tracers (DiTullio and Laws 1991; Duce and Tindale

1991; Hanson et al. 2001; Ho and Schanze 2020). Rain also mechanically perturbs the air–sea interface in a variety of ways (including but not only due to the surface buoyancy changes) and thereby modifies small-scale sea surface roughness and surface gravity waves with additional consequences for air–sea exchange (Schlössel et al. 1997; Zappa et al. 2009; Cavaleri et al. 2015; Cavaleri and Bertotti 2017, 2018; Laxague and Zappa 2020; Balasubramaniam and Ruf 2020). Rainfall also covaries with and depends on various other atmospheric variables, for example, the wind, air temperature, humidity, and properties of clouds (Rickenbach and Rutledge 1998; Tokay et al. 1999; Masunaga et al. 2005; Jin et al. 2018; Stephens et al. 2019; Iyer and Drushka 2021a), which also influence the downwelling shortwave and longwave radiation at the sea surface. As a consequence of the variable multitude of changes to the atmosphere and ocean that occur with rain and the intermittency of strong rain events, the characteristics of the surface atmosphere and upper ocean during rain events vary considerably in space and time and how the upper ocean responds to a rain event is not fully understood.

This study characterizes the surface atmosphere and upper-ocean physics during rainy days in the central equatorial Pacific, where we define a day to be rainy when the rainfall exceeds 24 mm in 24 h. Our focus on what we will see are

 Denotes content that is immediately available upon publication as open access.

Corresponding author: Daniel B. Whitt, daniel.b.whitt@nasa.gov

DOI: 10.1175/JPO-D-22-0033.1

For information regarding reuse of this content and general copyright information, consult the [AMS Copyright Policy \(www.ametsoc.org/PUBSReuseLicenses\)](https://www.ametsoc.org/PUBSReuseLicenses).

relatively infrequent days with more than 24 mm of rain is made possible by the availability of long-term in situ observations from the Tropical Atmosphere Ocean (TAO) moored buoy array that allow for a statistical analysis of rare rainy days. However, our focus on these rare days in which the rain exceeds 24 mm (as opposed to more frequent but less rainy days) is also motivated by comparison with the typical diurnal cycle of ocean buoyancy $b = -g\rho/\rho_{sw}$, where $g = 9.81 \text{ m s}^{-2}$ is the acceleration due to gravity, ρ is the potential density of the seawater, which varies with salinity and inversely with temperature, and $\rho_{sw} \approx 1025 \text{ kg m}^{-3}$ is the reference potential density (Fofonoff and Millard 1983). Specifically, the upper-ocean buoyancy b is typically strongly modulated by the diurnal cycle of shortwave radiation, in part because the winds and waves are of modest magnitude and variance (Young 1999; Whitt et al. 2019). The penetrating shortwave radiation on a typical (nonrainy) day in the region injects buoyancy at a rate

$$B_{\text{net}}^{\text{SW}} \approx \frac{g\alpha Q_{\text{SW}}}{\rho_{sw} c_p} \approx 7.7 \times 10^{-10} Q_{\text{SW}} (\text{m}^2 \text{ s}^{-3}), \quad (1)$$

where Q_{SW} is the surface heat flux (in W m^{-2} on the right hand side), $\alpha \approx 3.2 \times 10^{-4} \text{ }^{\circ}\text{C}^{-1}$ is the thermal expansion coefficient of seawater, and $c_p \approx 4000 \text{ J kg}^{-1} \text{ }^{\circ}\text{C}^{-1}$ is the specific heat of seawater. Averaged over a typical (nonrainy) day, $Q_{\text{SW}} \approx 200 \text{ W m}^{-2}$ and the time-integrated $B_{\text{net}}^{\text{SW}}$ is about $0.013 \text{ m}^2 \text{ s}^{-2}$. The net oceanic absorption of shortwave radiation is mostly compensated by heat losses due to net longwave, sensible, and latent fluxes at the surface, but these heat losses are spread fairly evenly across 24 h whereas the shortwave radiation is only during the daytime. Thus, there is a substantial diurnal cycle between positive (daytime) and negative (nighttime) net heat transfer from the atmosphere to the ocean and hence a corresponding diurnal cycle in upper-ocean buoyancy. To put 24 mm of rain in a day in the context of a typical diurnal cycle of buoyancy on a nonrainy day, convert the rain rate R to an effective surface buoyancy flux:

$$B_{\text{net}}^R \approx \frac{g\beta S_{\text{ref}} R}{\rho_{fw}} \approx 2.5 \times 10^{-4} R (\text{m}^2 \text{ s}^{-3}), \quad (2)$$

where R is in $\text{kg m}^{-2} \text{ s}^{-1}$ (or equivalently mm s^{-1}) on the right-hand side, $\beta \approx 7.4 \times 10^{-4} \text{ psu}^{-1}$ is the haline contraction coefficient of seawater, $S_{\text{ref}} \approx 35 \text{ psu}$ is the reference salinity of the seawater, and $\rho_{fw} \approx 1000 \text{ kg m}^{-3}$ is the density of freshwater. Then, observe that the time-integrated B_{net}^R associated with 24 mm ($=24 \text{ kg m}^{-2}$) of rain is about $0.006 \text{ m}^2 \text{ s}^{-2}$. Although 24 mm is a rather substantial amount of rain in a day, it yields less than half the buoyancy perturbation of the typical daytime shortwave radiation in the central equatorial Pacific. By focusing our attention on rains exceeding 24 mm in a day, we are focusing on rains that are expected to substantially perturb the buoyancy and hence physics of the boundary layer on a daily time scale. As we will see, such events are infrequent but do occur in the central equatorial Pacific Ocean. In addition, since a relatively large fraction of the total rain occurs in relatively rare strong rains (Pendergrass 2018), a substantial fraction of the total rain is expected to impact diurnal ocean boundary layer energetics even though the impacts are

infrequent (e.g., about 38% and 50% of all rain occurs on days with more than 24 mm of rain in TAO buoy observations on the equator at 155° and 170°W , respectively).

In contrast to most other studies of the surface atmosphere and upper-ocean response to rainfall in the tropical Pacific, this study focuses exclusively on the equator in the central Pacific (roughly 140° – 170°W). Most previous studies of rainfall in the equatorial Pacific have focused on the western Pacific warm pool to the west or the intertropical convergence zone to the north, where climatological rain rates are high (7 – 10 mm day^{-1}); the central equatorial Pacific, in contrast, typically experiences much less rainfall (1 – 3 mm day^{-1} on average) (Adler et al. 2017). However, the central Pacific is within the center of action for El Niño precipitation variability, and about 4 times more rain falls in the central equatorial Pacific during El Niño events than during La Niña events (Ropelewski and Halpert 1987, 1996; Trenberth and Caron 2000; Adler et al. 2017). In addition, since rainfall is intermittent, rainy days occur even during neutral or La Niña conditions in this region of climatologically weak rainfall.

Although this regional study adds to the general understanding of the surface atmosphere and upper-ocean dynamics during rainy days, our narrow focus on the central equatorial Pacific is specifically motivated by the unique and globally significant upper-ocean turbulence physics that is dominant within about $\sim 1^{\circ}$ of the equator in the central and eastern Pacific. This unique boundary layer physics (Moum et al. 1989; Lien et al. 1995; Moum et al. 2009; Smyth et al. 2013) arises because of the especially strong shear between the subsurface eastward Equatorial Undercurrent and the westward South Equatorial Current at the surface (but can also occur elsewhere in the equatorial oceans; see Pei et al. 2020; Cherian et al. 2021). The strong shear facilitates the transfer of kinetic energy to turbulence that drives strong vertical heat and momentum mixing below the surface mixed layer but with a diurnal cycle known as deep-cycle turbulence. Due to the strong vertical fluxes, deep-cycle turbulence significantly influences the sea surface temperature and momentum budgets, ocean circulation, and hence regional as well as global climate dynamics via atmospheric teleconnections (Gregg et al. 1985; Lien et al. 1995; Qiao and Weisberg 1997; Wang and McPhaden 1999; Moum et al. 2009, 2013; Holmes et al. 2019b; Deppenmeier et al. 2021). However, deep-cycle turbulence is crudely parameterized in regional and global ocean models (Zaron and Moum 2009) with consequences for the simulated ocean and climate dynamics (Meehl et al. 2001; Danabasoglu et al. 2006; Richards et al. 2009; Zhu and Zhang 2019; Holmes et al. 2019a). Specifically, it is unknown if and when a rain event might modify deep-cycle turbulence.

During a broader effort to simulate equatorial ocean surface boundary layer and deep-cycle turbulence in large-eddy simulations (LES; Whitt et al. 2022), the oceanic response to an infrequent rainy day was coincidentally simulated on the equator in the central Pacific during a period of slightly negative (but formally neutral) oceanic Niño index in early October 1985. Figure 1 shows time series of the rain rate from the Japanese atmospheric surface reanalysis (JRA55do; Tsujino et al. 2018) that forces three LES spanning 155° – 165°W on the equator. These simulations of

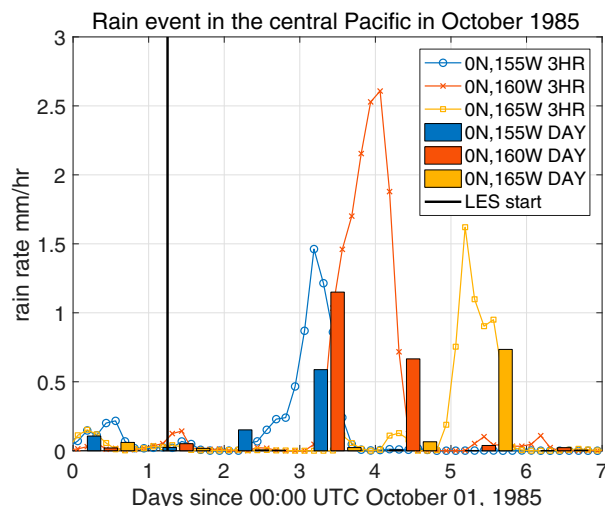


FIG. 1. Time series of the rain rate from the JRA55do atmospheric surface reanalysis during a rain event in the central equatorial Pacific at three longitudes along the equator as indicated in the legend. Rates are plotted as 3-hourly (line) and daily 0000–2400 UTC (bar) means. Local solar time is 10–11 h behind UTC, depending on the longitude. Note that all the LES begin at 0600 UTC 2 Oct (black line).

opportunity will ultimately provide some preliminary answers to the question of whether and how a rainy day might modify the typical diurnal deep cycle of equatorial turbulence. However, to put these simulations in context and aid in interpreting the results, the paper begins by characterizing the statistical properties of rainy days in the central equatorial Pacific Ocean, including their distribution in time and the accompanying atmospheric surface characteristics. Then, the paper describes the range of ocean conditions observed before rainy days as well as the observed oceanic responses to a rainy day. With that climatological and observational context, the paper describes the three simulated ocean responses to rain in LES. Finally, two observational examples of the ocean response to a rain event are presented, which are the only two known examples that include collocated surface meteorology, ocean temperature, salinity, and velocity profiles, as well as turbulent microstructure observations from χ pods on the equator in the central Pacific Ocean. However, the discussion focuses on the LES results, because the χ pods are only deployed at a few depths below the surface mixed layer.

2. Methods

The results are obtained via an analysis of atmospheric and oceanic observations collected from the TAO/TRITON mooring array, output from the JRA55do atmospheric surface reanalysis, as well as output from LES of the ocean surface boundary layer forced by the atmospheric reanalysis.

a. TAO mooring and buoy data

From the TAO data on the Global Tropical Moored Buoy Array (GT MBA) website (see the Data availability statement and McPhaden et al. 2010), we use daily-averaged rain rates to

identify rainy days along the equator at 170°, 155°, and 140°W. These daily rain rates are averaged from 0000 to 2400 UTC at all locations, and local solar times are 9–12 h behind UTC depending on the longitude. Although the 0000–2400 UTC averaging interval is a subjective choice, the alternatives are not obviously superior because climatological hourly rain rates are distributed fairly uniformly across the day with only a modest peak between midnight and sunrise. Hence, the standard published 0000–2400 UTC product is used for convenience and consistency.

From 0°N, 170°W, where rainy days are more frequent, we use the high-frequency 10-min rain, air temperature (at 2.2 m), relative humidity (at 2.2 m), and wind speed and direction (at 3.5 m) for further analysis. In addition, 2-min shortwave and longwave radiation data are used. Below the ocean surface, we use high-frequency hourly salinity, 10-min temperature (at 1-, 5-, 10-, 25-, and 50-m depth), as well as hourly velocities from the current meters (at 10- and 25-m depth) and the acoustic Doppler current profiler (ADCP) data (in 5-m bins from 30 m down). Only data with quality flags 1 or 2 are retained. From these high-frequency moored buoy observations at 170°W, air-sea fluxes are estimated from the atmospheric and 1-m-deep ocean observations using the bulk formulas in the COARE algorithm (the coare35vn MATLAB code; see Fairall et al. 2003; Edson et al. 2013).

b. Surface analyses

We use version 1.3 of the atmospheric surface reanalysis JRA55do (Tsujino et al. 2018). This product spans 1958 through 2018 at 3-hourly (in UTC) and nominally 0.5° resolution and includes the downwelling surface shortwave and longwave radiation, the rain rate, the sea level pressure, as well as the wind speed and direction, air temperature, and specific humidity 10 m above the sea level. Leap days are omitted, hence two rainy days near leap days are also excluded from the analysis in section 3b below. As the near-equatorial grid points are located about 1/4° north and south rather than on the equator, these nearest points are averaged to estimate the value on the equator.

We also use sea surface temperature analyses. The monthly 1° resolution product Centennial In Situ Observation-Based Estimates Sea Surface Temperature (COBE-SST; Ishii et al. 2005) is used to estimate surface fluxes from the JRA55do atmospheric surface fields (as in Tsujino et al. 2018) using the same bulk formulas that are applied to the TAO observations (the coare35vn MATLAB code; see Fairall et al. 2003; Edson et al. 2013). There are errors in these flux estimates due to errors in the estimated atmospheric and ocean states, in addition to uncertainties in the bulk flux formulas. The former is constrained by comparing the flux estimates from the reanalysis with the flux estimates directly from the TAO data. On seasonal and longer time scales, rain in the central equatorial Pacific is strongly correlated with El Niño (Ropelewski and Halpert 1987, 1996; Trenberth and Caron 2000; Adler et al. 2017), so we also use the NOAA/NCEP monthly Oceanic Niño Index (ONI) from 1958 to 2018, which is a 3-month running mean of ERSST.v5 sea surface temperature anomalies in

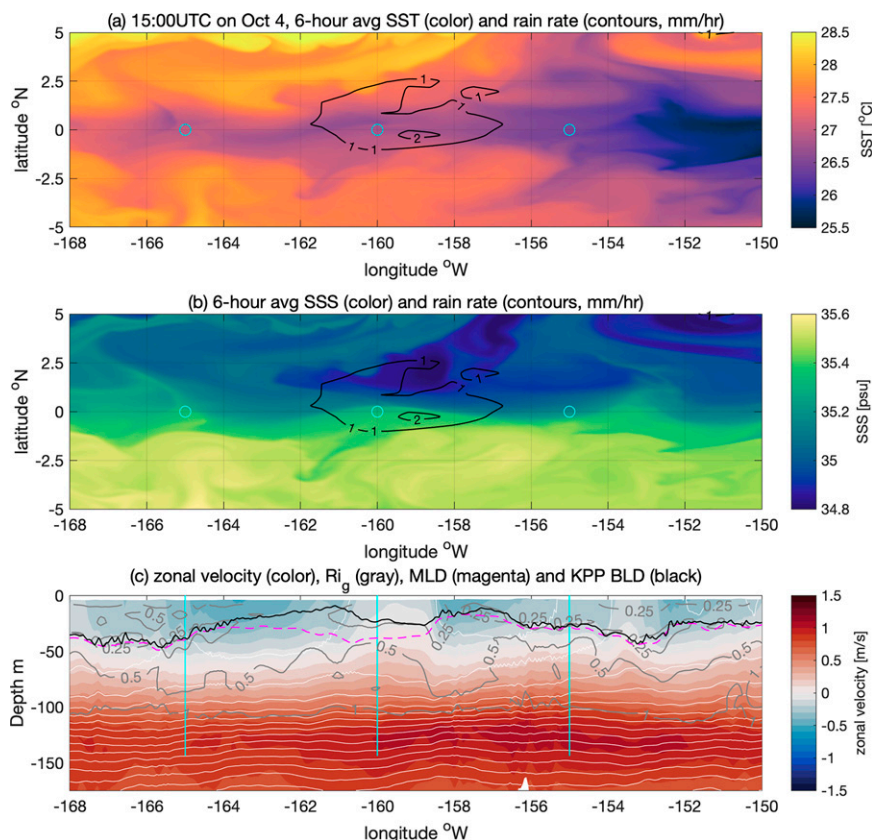


FIG. 2. The larger-scale ocean context for the LES is from a $1/20^\circ$ resolution regional ocean model of the central and eastern equatorial Pacific Ocean. The plots include 6-h averages of (a) sea surface temperature and (b) salinity with rain rate contours overlaid in black during the period simulated by LES. (c) In addition, a depth–longitude section shows the zonal velocity (color), potential density (white contours every 0.2 kg m^{-3}), gradient Richardson number Ri_g (gray contours, after smoothing with a 5-point/27.5-km zonal average), KPP surface boundary layer depth [black, defined as in Large et al. (1994)], and mixed layer depth (dashed magenta, defined by the first depth level where the potential density is 0.015 kg m^{-3} denser than the surface level, and smoothed with a 5-point/27.5-km zonal average). The snapshots are at 1500 UTC, i.e., 0400–0500 local time depending on the longitude. Cyan circles in (a) and (b) and lines in (c) indicate the LES locations.

the Niño 3.4 region relative to centered 30-yr base periods updated every 5 years (Huang et al. 2017).

c. Large-eddy simulations

This study presents results from three LES from a broader array of simulations of equatorial upper-ocean turbulence. These three runs are hindcasts representative of roughly 2–8 October 1985 at 165° , 160° , and 155°W along the equator (for the mesoscale oceanic context, see Fig. 2). The configurations are very similar to those of Whitt et al. (2022). Although the protocol and code are essentially the same, there are two main differences. First, these LES are in different locations than those reported in Whitt et al. (2022) and hence have different boundary conditions, initial conditions, and large-scale tendencies which are published in the configuration files (Whitt 2022b). Second, the domain is deeper in these runs, since the simulations are further west (144 versus 108 m).

Otherwise, the methodology is the same as in Whitt et al. (2022).

To briefly review, the LES (originally developed by Taylor 2008) solve the nonhydrostatic Boussinesq equations with a Smagorinsky-type closure to represent subgrid-scale mixing in a horizontally periodic $306 \text{ m} \times 306 \text{ m} \times 144 \text{ m}$ deep domain spanned by a uniformly spaced $0.85 \text{ m} \times 0.85 \text{ m} \times 0.5 \text{ m}$ resolution grid. The subgrid Prandtl number increases with the gridscale Richardson number according to a formula from Anderson (2009), and the subgrid-scale diffusivity of salinity, temperature, and buoyancy are the same. Thus, the LES resolve the outer scales of the turbulence and provide insight into the turbulence physics without strong sensitivity to the subgrid closure, although there is an implicit assumption that the buoyancy Reynolds number is sufficiently large and hence the dynamics of molecular mixing are not too important (which is typically true in the boundary layer,

but see [Walesby et al. 2015](#)). In all cases, the LES begin at 0600 UTC 2 October 1985 and run for 5–7 simulated days. The LES are forced at the surface by 6-hourly surface fluxes of momentum, salt, and heat (including penetrating shortwave radiation), which are read in from a file. The fluxes were derived using the bulk flux algorithms of [Large and Yeager \(2009\)](#) in a $1/20^\circ$ resolution regional ocean hindcast of the central and eastern equatorial Pacific in the regional ocean modeling system ([Shchepetkin and McWilliams 2005](#); [Haidvogel et al. 2008](#)) forced by the JRA55do reanalysis (as described in [Whitt et al. 2022](#)). Rain and evaporation are represented as virtual salt fluxes at the surface boundary in the LES; there are no explicit freshwater or volume changes, and the model formally has a rigid top and bottom. There is an implicit assumption that surface gravity waves only modestly alter the turbulent transports, which is motivated by the weak winds and small waves (with 1–2-m significant heights) in the region (see [Young 1999](#); [Babanin 2006](#); [Echevarria et al. 2019](#)). But, waves almost certainly have some effect, which should be quantified in future work. In addition, the horizontally averaged profiles of temperature and momentum in the LES evolve due to the large-scale (i.e., averaged 15 km horizontally, 8 m vertically, and 6 h temporally) tendencies of temperature and momentum associated with advection and the pressure gradient force from the regional model (the large-scale salinity tendency is set to zero in the LES). The bottom temperature and horizontal momentum are set to fixed constants, which are chosen based on the initial conditions at each respective location. The bottom boundary condition does not significantly influence the interior evolution of the velocity and temperature profile due to the large-scale interior tendencies and the fixed small diffusivity and viscosity at the bottom boundary. The time evolution of the surface and interior forcing and the resulting horizontally averaged statistics from the LES are saved and published online ([Whitt 2022c,d](#)).

d. Ocean turbulence observations on TAO moorings during rainy days

Direct measurements of turbulent fluctuations are sparse in the ocean, but the central equatorial Pacific, specifically 0°N , 140°W , is relatively well observed due to the multidecade deployments of Oregon State University χ pods on the TAO mooring. The χ pods measure turbulent temperature fluctuations that can be used to estimate the turbulent vertical heat flux ([Moum and Nash 2009](#); [Perlin and Moum 2012](#); [Moum et al. 2013](#); [Warner and Moum 2019](#); [Cherian et al. 2020](#); [Smyth et al. 2021](#); [Moum 2021](#)). Although rainy days are exceptionally rare at 140°W , occurring only a handful of times in the entire observational record from the TAO buoys, χ pods were deployed during two rainy days (12 April and 19 June) during the 2015 El Niño. In both of these events, the rain exceeded 24 mm in 24 h (by definition), and about 35 mm of total rain fell in a 48-h period. However, all 35 mm occurred in a single 4-h high-intensity event in April, whereas the rain was spread across several shorter and less-intense events with a 24-h maximum just exceeding 24 mm in June.

Data revealing the ocean–atmosphere response during these two events are taken from the GTMBA website (see the Data availability statement and [McPhaden et al. 2010](#)). Subsurface turbulent heat fluxes are taken from the shallowest available χ pod data during each rainy day (at 29- and 69-m depth in April and June, respectively). These turbulence observations are contextualized with subsurface temperature and salinity observations from the 10-min and hourly products, respectively, which are available at 1, 5, 10, 20, 40, 60, and 80 m for both variables and additionally at 25 and 45 m for temperature. Zonal and meridional velocity are derived by merging the hourly current meter observations (at 10, 25, 40, and 80 m) and the hourly ADCP data (in 5-m bins below 30 m). The velocity observations are mapped to a single 2.5-m vertical grid using biharmonic spline interpolation, where time is scaled so that one hour has a “distance” equal to 10 m in the vertical. Temperature and salinity are interpolated to the uniform 2.5-m depth grid using cubic splines. From that uniform grid, a mixed layer depth is calculated as the shallowest depth where the potential density ρ is 0.015 kg m^{-3} denser than the vertically averaged potential density in the top 10 m (this definition of the MLD is used throughout this paper). In addition, the gradient Richardson number is calculated from the buoyancy and horizontal velocity,

$$\text{Ri}_g = \frac{N^2}{S^2} = \frac{\partial b / \partial z}{(\partial u / \partial z)^2 + (\partial v / \partial z)^2}. \quad (3)$$

During these rain events at 140°W , hourly air–sea fluxes are available directly from the GTMBA website, including the net air–sea heat flux Q_{net} , the net freshwater flux $F_{\text{fw}} = R - E$ (rain minus evaporation), and the surface stress $|\tau|$. The surface shortwave radiation is from the 2-min product. Heat and freshwater fluxes are converted to buoyancy fluxes, where $B_{\text{net}} = B_{\text{net}}^S + B_{\text{net}}^T$ is a sum of salinity (virtual salt flux) and temperature contributions,

$$B_{\text{net}}^S = \frac{g\beta S_{\text{ref}} F_{\text{fw}}}{\rho_{\text{fw}}}, \quad \text{and}$$

$$B_{\text{net}}^T = \frac{g\alpha Q_{\text{net}}}{\rho_{\text{sw}} c_p}.$$

3. Observations of the surface atmosphere and upper-ocean during rainy days

a. Frequency and spatiotemporal distribution of rainy days in the central Pacific

Following, e.g., [Allen and Ingram \(2002\)](#), the frequency of rainy days ($>1 \text{ mm h}^{-1}$ on average or 24 mm day^{-1}) is quantified and contextualized in a log–log plot showing the upper half of daily rain quantiles from the TAO buoy data and the JRA55do reanalysis at several longitudes along the equator in the central Pacific ([Fig. 3](#)). The distributions are all qualitatively similar and consistent with the climatological distribution of mean rainfall, in that rain rates are lower to the east at all quantiles shown. For example, the TAO observations

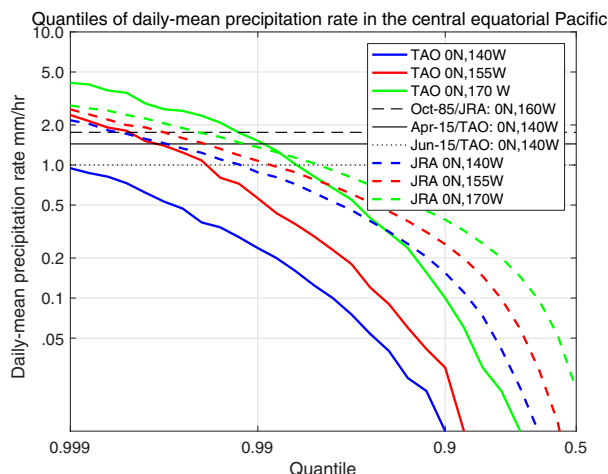


FIG. 3. Quantiles of the daily (24-h-average) rain rates at three central Pacific sites along the equator (as indicated in the legend) are derived from the TAO buoy data (solid lines) and the JRA55do reanalysis (dashed lines). For reference, the horizontal black lines indicate the maximum average rain rate (in any 24-h window) in the events with available simulations or observations of turbulence, including the simulated event at 0°, 160°W in October 1985 (cf. Fig. 1), and the observed events in April and June 2015 at 0°, 140°W.

indicate that rainy days > 24 mm occur only once every few years at 140°W and a handful of times every year at 170°W on average. However, the TAO buoy observations have notably more rain in the extremes and more variation as a function of longitude than the JRA55do reanalysis. The TAO data and the JRA55do reanalysis are not expected to be exactly the same, since the reanalysis represents an average over roughly 6000 km² and extends further back in time, but the distributions do show that the simulated rain event in early October 1985 in the JRA55do (Fig. 1) is plausible even without direct observations to verify the amount of rainfall during this particular event. In addition, these distributions put the October 1985 rain event in context. The peak daily-average (0000–2400 UTC) rain rate of 1.2 mm h⁻¹ at 160°W is between the 99th and 99.9th percentile of daily-average rain rates at 155°W, and between the 97th and 99th percentiles at 170°W. In addition, the maximum 24-h-average rain rate at 160°W (without regard to hours) is between the 99th and 99.9th percentiles at both 155° and 170°W. Hence, a rain event like the one at 160°W in Fig. 1 occurs infrequently, on the order of once in 100 days.

However, the seasonal and interannual distributions of rainfall events exceeding 24 mm day⁻¹ (1 mm h⁻¹ on average) at 170°W demonstrate that the event shown in Fig. 1 is actually more unusual than the quantile distributions suggest, because this event occurs in October and during a slightly negative ONI (Fig. 4). In general, rainy days occur more frequently during a positive ONI and more than twice as frequently from December through February compared to October. These results in Fig. 4 are qualitatively consistent with the interannual and climatological seasonal variations in

total rainfall (e.g., Adler et al. 2017). Hence, a rainfall event like this one in boreal autumn with slightly negative ONI as in Fig. 1 effectively occurs less frequently than once in 100 days.

b. Atmospheric surface properties during rainy days

The ocean response during and after a rainy day depends on not only the rain rates but also the net air–sea heat, fresh-water, and momentum fluxes, which in turn depend on the atmospheric surface air temperature, humidity, and wind speed among other factors (e.g., Fairall et al. 2003; Large and Yeager 2009). Figure 5 quantifies several of these complementary changes in atmospheric surface variables in composite rain events and distributions across all rainy days at 170°W in the JRA55do reanalysis and the high-frequency TAO buoy data. The JRA55do and TAO data are consistent. Rain rates are elevated to about 1–3 mm h⁻¹ on average during the rainy day, much higher than the days before and after. The rain rate peaks during the nighttime and is slightly higher from 0000 to 0600 local time (Fig. 5a), consistent with the mean diurnal cycle of rain rates which has an amplitude of 1 mm day⁻¹, from 2.8 to 3.8 mm day⁻¹, averaged over every day of the 61 years of 3-hourly JRA55do data (not shown). In addition, downwelling shortwave radiation is reduced by about 50 W m⁻² on average over 24 h and by 200–300 W m⁻² during the daytime at the end of the rainy day (i.e., at hour 12 in Fig. 5b). The air temperature is reduced by about 1°C, the relative humidity is increased by about 5% (consistent with consequences of the lower air temperature for the saturation vapor pressure via the Clausius–Clapeyron relation), and both extrema are achieved between 0000 and 0600 local time (Figs. 5d,e). The climatological westward (easterly) zonal wind weakens on average during the rainy day (Fig. 5c). A corresponding reduction in the wind speed and wind stress occurs on average across the JRA55do rain events but is insignificant across the TAO data (not shown).

In all the atmospheric surface variables, but particularly the wind speed, there is considerable variability between rainy days (Fig. 5). The corresponding distributions of the daily average rain rates range from about 1 to 5 mm h⁻¹ (24–120 mm day⁻¹). Daytime downwelling shortwave radiation anomalies, which are most prominent at the end of the rainy day (i.e., at hour 12 in Fig. 5b), range from large reductions of -1000 W m⁻² to substantial increases of $+500$ W m⁻² relative to daytime before the rainy day. And, 24-h daily average downwelling shortwave radiation anomalies range from about -150 to $+100$ W m⁻². Daily air temperature anomalies range from about -3° to $+1.5^{\circ}$ C, and daily relative humidity anomalies range between about -7.5% and $+15\%$. Hence, the individual rain events vary considerably around the multievent composite.

For the composite upper-ocean buoyancy dynamics, the most important, systematic, and complementary change in the atmospheric surface variables is the reduction in downwelling shortwave radiation, which compensates for the freshening due to rain in the net air–sea buoyancy flux (Fig. 6). Averaged across all rainy days, the net heat flux into the ocean is reduced by 47 W m⁻² (JRA55do) and 52 W m⁻² (TAO) relative to nearby days, and shortwave radiation anomalies

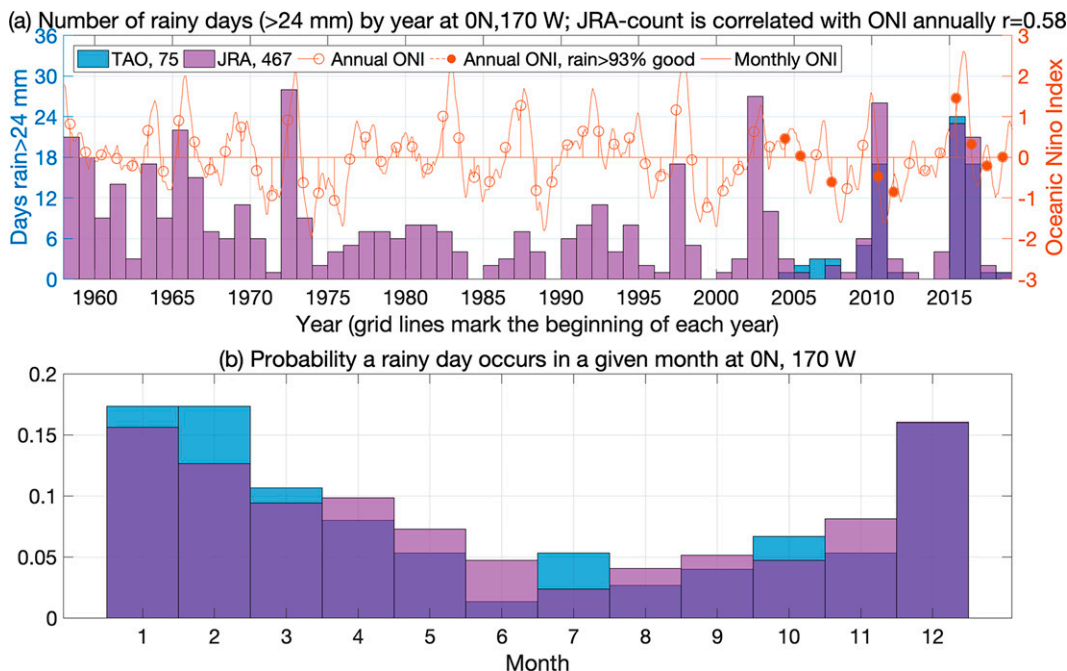


FIG. 4. (a) Interannual and (b) seasonal distributions of rainy days (identified by more than 24 mm in 24 h) at 0° , 170° W are derived from the TAO data (blue) and the JRA55do reanalysis (purple). The frequency of rainy days is correlated with El Niño (positive ONI), as expected. The total number of rainy days by this definition is 75 for the daily TAO data and 467 for the JRA55do reanalysis. The bar heights in the probability distributions are normalized so that they sum to one.

[45 W m^{-2} (JRA55do) and 40 W m^{-2} (TAO)] are the dominant cause of the net anomalies. The sensible heat flux [5 W m^{-2} (JRA55do) and 8 W m^{-2} (TAO)] and the rain itself [4 W m^{-2} (JRA55do) and 6 W m^{-2} (TAO)] tend to modestly strengthen these net heat flux anomalies, while longwave radiation and latent heat flux tend to weaken the anomalies [by 1 W m^{-2} (JRA55do) and 5 W m^{-2} (TAO) for longwave, and by 6 W m^{-2} (JRA55do) and insignificantly (TAO) for latent]. Averaged across all rain events, the reduction in shortwave radiation during the daytime at the end of the rainy day (i.e., under the yellow bar in Fig. 6) yields a stronger reduction in the stabilizing net surface buoyancy flux associated with temperature effects B_{net}^T than the concomitant increase in the net stabilizing buoyancy flux associated with the rain and salinity effects B_{net}^S . As a result, B_{net} is reduced during the daytime at the end of the rainy day on average across all rain events (Figs. 6 and 7). Combining temperature and salinity effects, the daytime buoyancy flux $B_{\text{net}} = B_{\text{net}}^T + B_{\text{net}}^S$ (under the solid yellow bar in Fig. 6) is stabilizing on all but one of 465 rainy days in the JRA55do data and on all but 7 of the 29 (24%) rainy days with valid buoyancy fluxes in the TAO data. Destabilizing daytime buoyancy fluxes occur when the shortwave radiation is strongly suppressed, and the stabilizing rain is insufficient to overcome net buoyancy loss associated with other contributions to the net flux. During nighttime (under the solid black bar in Fig. 6), the stabilizing effect of precipitation yields $B_{\text{net}}^S > 0$ and compensates the destabilizing surface heat flux $B_{\text{net}}^T < 0$ that typically drives nighttime convection in the ocean. The rain is not sufficient on average

across rain events to produce a stabilizing net buoyancy flux $B_{\text{net}} > 0$ at night, but on 33% (JRA55do) to 38% (TAO) of rainy days the nighttime buoyancy flux is stabilizing rather than destabilizing (Fig. 7a), in which case convection is suppressed in the ocean boundary layer. The net effect of these changes is higher B_{net} into the ocean and a suppressed diurnal cycle in B_{net} on average during a rainy day: the stabilizing positive buoyancy flux is reduced during the daytime, but the destabilizing negative buoyancy flux is increased to a greater degree at nighttime [qualitatively similar compensation is found elsewhere, e.g., in the western Pacific warm pool as reported in Anderson et al. (1996)].

c. Oceanic mean conditions during rainy days

The next section quantifies the ocean response to rainy days by subtracting a 4-day moving average, because the upper-ocean salinity, temperature, and velocity profiles vary considerably between rain events for unrelated reasons thereby obscuring the forced response to the rainy day. In preparation for that analysis, this section quantifies the 4-day mean oceanic conditions during the observed rainy days at 0° , 170° W for context (Fig. 8; note the interannual and seasonal distribution of rainy days in Fig. 4). We find that salinity varies from about 34 to 35.5 psu above 100-m depth. And, the interquartile range is about 0.5 psu at any of these depths. Temperatures range from about 26° to 31°C at 1-m depth and from about 22° to 30°C at 100 m. The interquartile range is about 0.5°C at 1 m and 3°C at 100 m. The zonal velocities take both signs at all depths above 125 m and range from about -1.25 to $+1.25 \text{ m s}^{-1}$. The

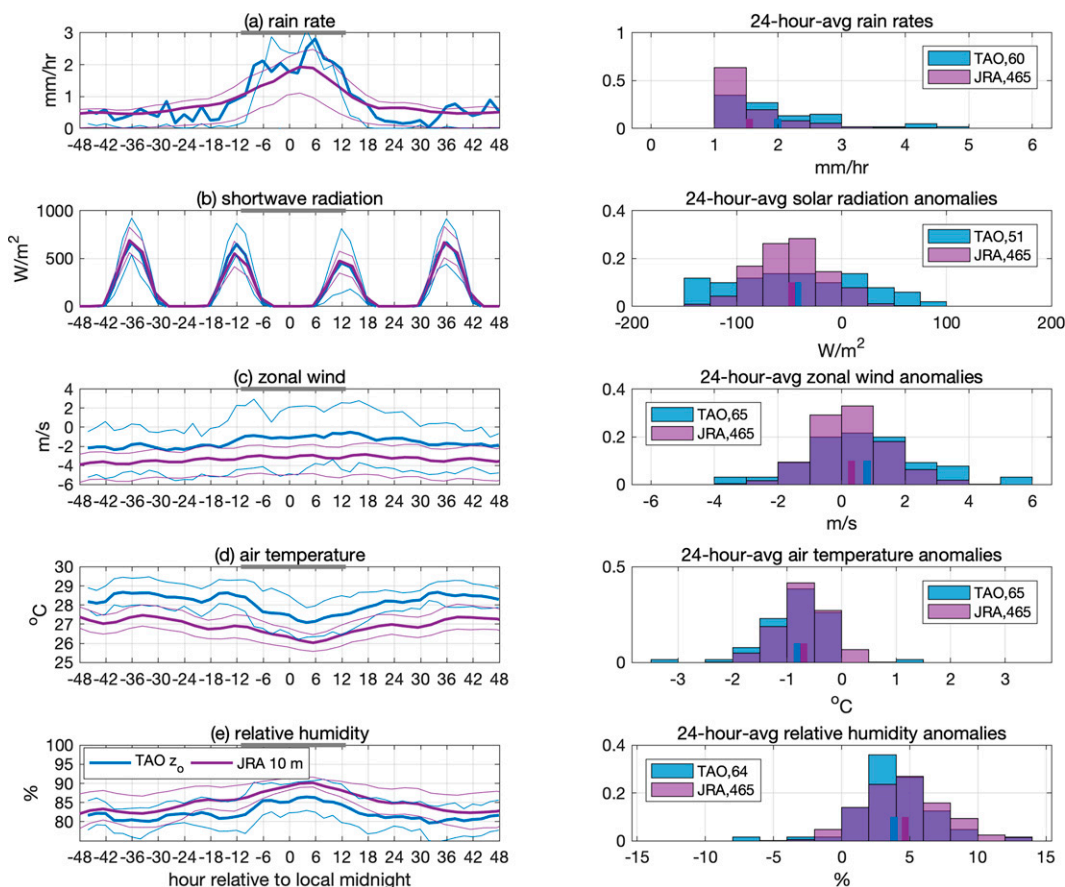


FIG. 5. (left) The TAO (blue) and JRA55do (purple) data are aggregated into composite time series showing how the atmospheric conditions at 0°, 170°W evolve on average (thick lines) during a 4-day window surrounding a rainy day (which is defined by more than 24 mm of rain under the gray bar, i.e., from 0000 to 2400 UTC). The time axes are zero at local midnight (about 1100 UTC). The thin lines bracket the interquartile ranges. (right) Distributions of the 24-h averages during each rainy day (i.e., under the gray bars) along with the number of included rain events, which varies depending on the data stream. Among the distributions, in (a) the rain rates are simply the 24-h average rain rates during each rainy day, whereas in (b)–(e) the distributions are rainy-day anomalies, which are calculated as differences from the conditions averaged over the other days in the 4-day window around each rainy day. Tick marks indicate the mean of each distribution. The rainy-day anomalies are similar in the JRA55do and TAO data, but there are notable differences between the 4-day mean of the composite wind speed, air temperature, and humidity, which arise from different spatiotemporal sampling and/or bias. Scaling the buoy data from the sample height $z_o = 2\text{--}4$ m to the nominal 10-m height of the JRA55do data increases the magnitude of wind speed by about 7% and reduces temperature and humidity by about 1% and cannot fully explain these differences.

interquartile range is about 0.5 m s^{-1} at any given depth above 125 m. In general, the observed median temperature and zonal velocity profiles during rain events are more consistent with El Niño than the climatological mean or La Niña, as expected (cf. Johnson et al. 2002).

Previous studies (e.g., Pacanowski and Philander 1981; Peters et al. 1988; Lien et al. 1995; Smyth and Moum 2013; Pham et al. 2017) have shown that the squared vertical shear of horizontal velocity S^2 , the vertical buoyancy gradient N^2 , and the gradient Richardson number $Ri_g = N^2/S^2$ are important constraints on and indicators of the upper-ocean turbulence in the eastern equatorial Pacific (although there remains active debate about the details). Although there is

significant (unquantified) uncertainty in these variables as measured with a sparsely sampled mooring, Smyth and Moum (2013) suggest that the median Ri_g from hourly data may in fact be relatively robust to these sampling limitations. Hence, Figs. 8d–f show profiles of the medians and interquartile ranges of S^2 , N^2 , and Ri_g across all the rain events. We find that the medians $S^2 \sim N^2 \sim 10^{-4} \text{ s}^{-2}$ are both strong as expected and decline by about an order of magnitude from $10^{-3.5}$ to $10^{-4.5} \text{ s}^{-2}$ from 110- to 25-m depth. However, compared to S^2 , N^2 is somewhat stronger at 110 m and somewhat weaker at 25 m such that the median gradient Richardson numbers range from about 1 at 110 m to 0.25 at 25 m. That is, there is an indication of strong

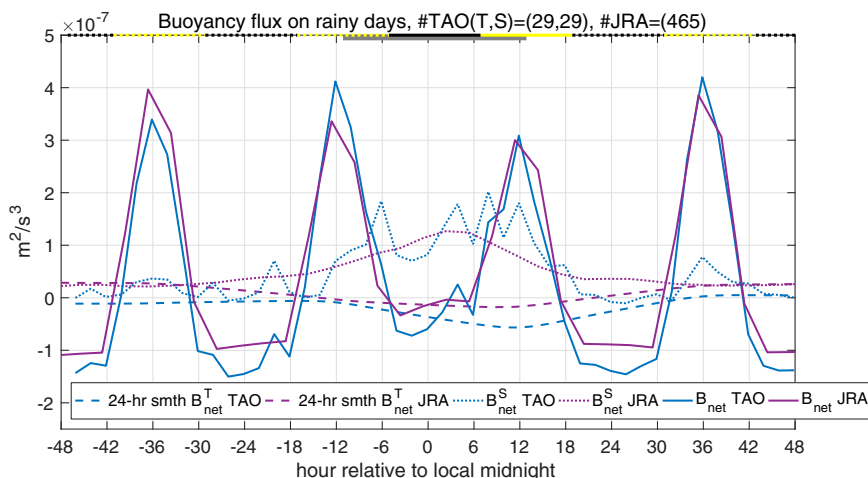


FIG. 6. The TAO (blue) and JRA55do (purple) data are aggregated into composite time series of the net downward surface buoyancy flux B_{net} averaged over all rain events at 0° , 170°W (which are defined by more than 24 mm of rain in the 24 h under the gray bar, i.e., 0000–2400 UTC). The time axis is zero at local midnight on the rainy day (about 1100 UTC). The buoyancy flux is also decomposed into contributions associated with temperature B_{net}^T (dashed lines) and salinity B_{net}^S (dotted lines). The temperature contribution B_{net}^T is smoothed with a 24-h moving average to filter out the diurnal cycle and facilitate comparison with the salinity contribution B_{net}^S , which has a negligible diurnal cycle. The number of events incorporated in each composite is indicated in the panel title. The solid black and yellow bars on the top axis indicate the primary nighttime and daytime windows referred to in Fig. 7, and the dotted black and yellow bars indicate the alternate nighttime and daytime windows that are subtracted to obtain nighttime and daytime anomalies associated with a rainy day.

shear, strong stratification, and marginal instability at about 25 m, which is suggestive of deep-cycle turbulence (Smyth and Moum 2013).

For future reference, note that the LES mean profiles of temperature, salinity, and velocity at 160°W differ considerably from the median profiles observed at 170°W (Fig. 8; see also Fig. 2). These differences are likely attributable to the fact that the LES is during a period of slightly negative rather than positive ONI and located 1000 km east of the observations (cf. Johnson et al. 2002). However, the simulated shear, stratification, and Richardson number profiles are qualitatively similar to the observations, suggesting that the turbulent response to a rainy day in the LES is plausibly similar to a typical turbulent response to a rainy day at 170°W .

d. Oceanic response to the rain in observations

As we will see, the typical observed temperature and salinity anomalies due to a rainy day in the high-frequency TAO mooring observations at 0° , 170°W are about 3–5 times weaker than the interquartile range of the unrelated slow (>4 day) oceanic variability described in the previous section. Hence, the forced ocean response to a rainy day is quantified in this section as an anomaly from a 4-day moving average representing the unrelated slow evolution of the ocean. With this approach, the composite upper-ocean salinity, temperature, and buoyancy anomalies are statistically significant, with 95% confidence in a bootstrap analysis

assuming each rain event is independent (Figs. 9 and 10). These significant oceanic anomalies tend to lag the atmospheric anomalies by several hours and are clearest near the surface. Each of the salinity, temperature, and zonal velocity responses during the rain events will be discussed in turn.

1) SALINITY

Although the data from a few infrequent strong rain events is not sufficient to quantify the slight diurnal cycle in upper-ocean salinity (Drushka et al. 2014), the data do clearly quantify a significant salinity response to rain events: salinity is anomalously low for about 24 h from nighttime during the rainy day to nighttime following the rainy day (from about 0 to 24 h in Fig. 9). The event-average composite and individual-event extreme salinity anomalies are surface intensified and most negative at the shallowest sensor at 1 m (Figs. 9 and 10). At 1 m, the composite event-average anomaly is more negative than -0.1 psu for about 12 h in the daytime during and following the rain, from hours 6 to 18 in Fig. 9. The 24-h-average anomalies range from about -0.4 to $+0.1$ psu with a mean of about -0.1 psu. A fresh salinity anomaly is also present at 5-m depth throughout the daytime following the rain (as at 1 m), but the composite anomaly is weaker (about -0.04 psu at 5 m compared to -0.1 psu at 1 m) and the distribution of 24-h anomalies is more tightly clustered around the mean. At the deeper sensors at 10 and 25 m, the salinity anomaly emerges later after the rain and is weaker than at the 1- and 5-m sensors. The relatively late emergence of fresh

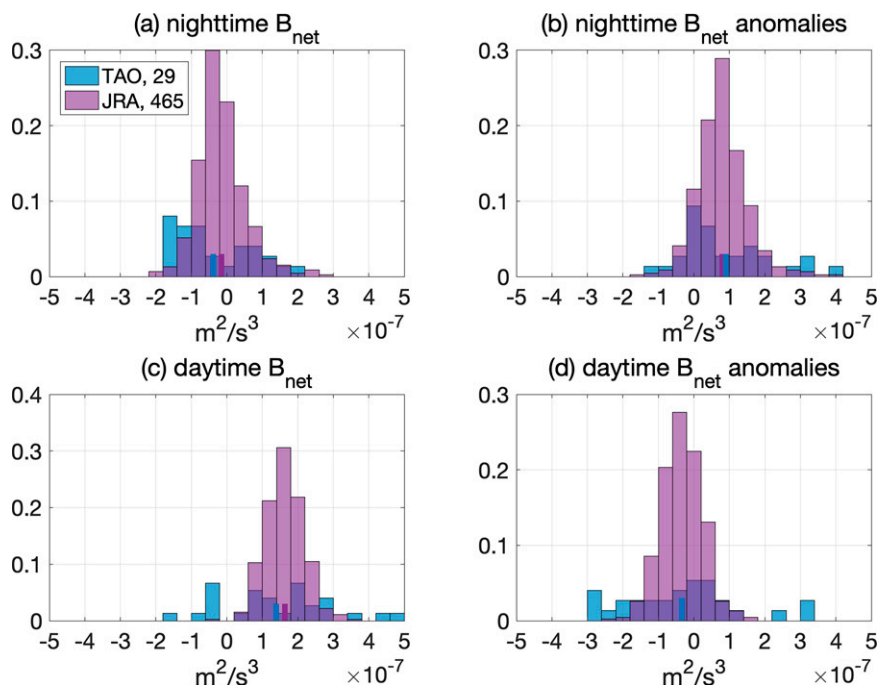


FIG. 7. Histograms (blue from TAO and purple from JRA55do) show (a) the distributions of the nighttime average (under the solid black bar in Fig. 6) and (c) the subsequent daytime average (under the solid yellow bar in Fig. 6) surface buoyancy flux B_{net} during each rain event as well as (b),(d) the corresponding anomalies relative to the other days in each 4-day window around the rain event. Alternate nighttime and daytime windows are indicated by the dotted black and yellow bars in Fig. 6. The bar heights in each histogram are normalized so that they sum to one. Tick marks indicate the mean of each distribution.

salinity anomalies at these deeper depths is qualitatively consistent with the expected evening descent of a shallow daytime warm/rain mixing layer due to stabilizing surface buoyancy flux B_{net} , relatively modest winds, and hence a relatively a small daytime Monin–Obukhov length scale (Monin and Obukhov 1954), which is a scaling for the depth where the stabilizing buoyancy forcing overcomes the destabilizing wind forcing and can sometimes be useful for predicting the depth of daytime rain/warm layers (Thompson et al. 2019).¹

A back-of-the-envelope calculation shows that these composite fresh upper-ocean salinity anomalies are quantitatively consistent with the composite net freshwater flux anomaly that occurs in conjunction with the rain (Fig. 6). In particular, a salinity anomaly of -0.1 psu integrated over a 10-m surface warm/rain layer is equivalent to a depth-integrated buoyancy anomaly of about $+0.007 \text{ m}^2 \text{ s}^{-2}$. Time-integrating the composite surface buoyancy flux anomaly associated with precipitation and evaporation B_{net}^S in Fig. 6, which is about $+5 \times 10^{-8} \text{ m}^2 \text{ s}^{-3}$ averaged over 48 h, yields a very similar $+0.009 \text{ m}^2 \text{ s}^{-2}$ depth integrated buoyancy anomaly (see also Fig. 9d).

¹ Throughout the paper, the buoyancy flux used in the calculation of the Monin–Obukhov depth is B_{net} minus the contribution from solar radiation that penetrates below that depth (Large et al. 1994).

2) TEMPERATURE

In contrast to salinity, the diurnal cycle is a dominant feature of the high-frequency temperature anomalies before, during and after the rain events (Fig. 9b; cf. Fig. 9a). The maximum of the composite positive diurnal temperature anomaly at 1 m is about $+0.16^\circ\text{C}$ before the rain event, and the peak to trough amplitude of the diurnal cycle at 1 m is about 0.23°C . Before the rain, the maximum 1 m composite diurnal temperature anomaly occurs in the late afternoon (e.g., hour -33 in Fig. 9), and the minimum 1 m composite diurnal temperature occurs at just about daybreak (e.g., hours -42 and -18 in Fig. 9). There are weaker but significant diurnal cycles in temperature at 5- and 10-m depth. But, the temperature composites in Fig. 9 do not reveal a significant diurnal cycle at 25 m or deeper, presumably because of the small number of rainy days and the confounding nondiurnal high-frequency variability, e.g., due to internal waves. Before the rainy day, the diurnal cycle composites from the upper 10 m of the 170°W mooring data in Fig. 9b are qualitatively similar to composites at 155°W and 180° reported by Masich et al. (2021) (which were created with much more data and without regard to rain events). However, Masich et al. (2021) also report a modest but significant diurnal cycle with a peak-to-trough amplitude of about 0.06°C at 25-m depth at 155°W, presumably because of the greater number of days they composited.

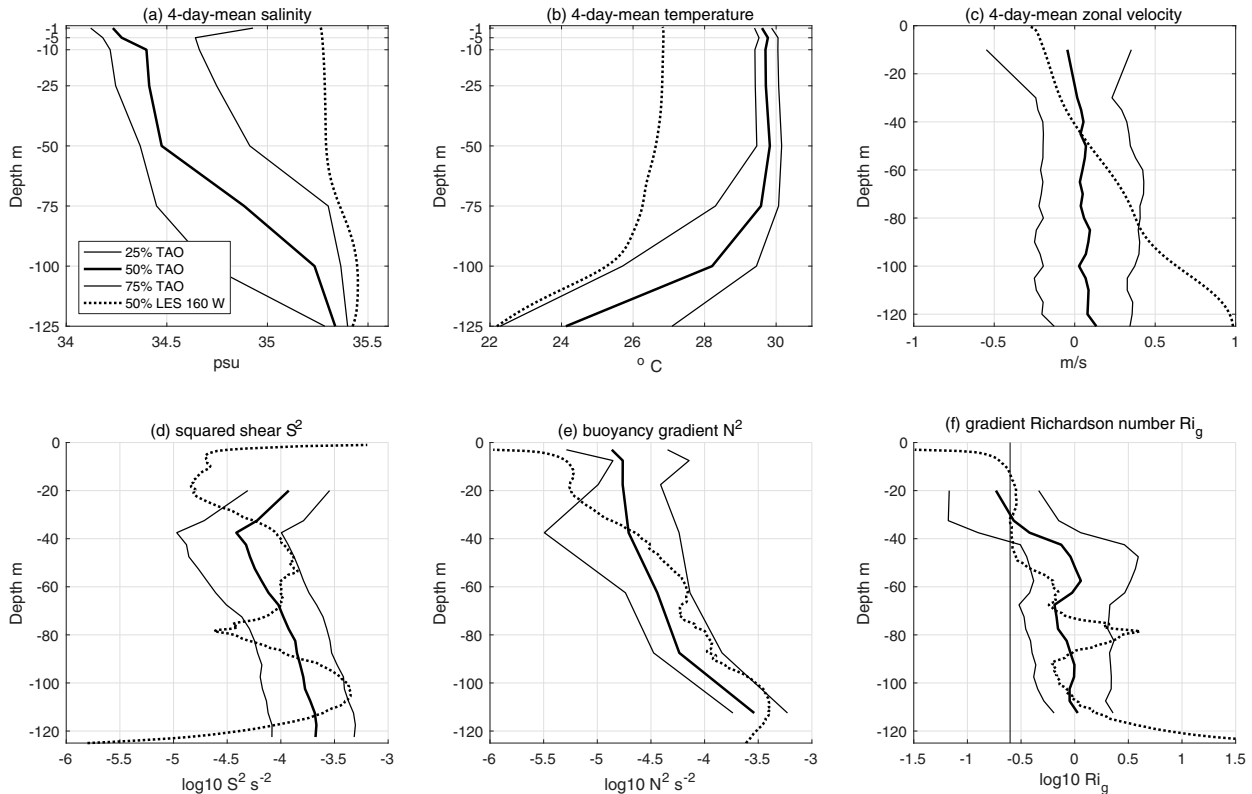


FIG. 8. (a)–(c) Medians and interquartile ranges of 4-day-mean ocean profiles of the salinity, temperature, and zonal velocity during the rain events observed in the TAO moored buoy data from 0° , 170°W . (d)–(f) Medians and interquartile ranges of the squared vertical shear, vertical buoyancy gradient, and gradient Richardson number derived from the 2-hourly binned observations across all rain events (i.e., without applying a 4-day mean to each event beforehand). For reference, the analogous LES profiles at 160°W are given by the black dotted lines. The y-axis grid lines indicate the depths where the observations are collected in (a) and (b). And, $\text{Ri}_g = 1/4$ is indicated by a vertical line in (f).

Subtracting the diurnal cycle (defined from -48 to -24 h) before each rain event from each high-frequency temperature anomaly time series and then compositing yields the characteristic nondiurnal high-frequency temperature anomalies during a rain event in Fig. 9c. This nondiurnal composite highlights the clear and significant temperature response to the rain event, which is qualitatively very similar to the salinity response (cf. Figs. 9a,c). Relative to the diurnal cycle before the rainy day, the near-surface temperature becomes significantly cooler at about daybreak following the rainy day (hour 6 in Fig. 9c). It may be noted that the composite temperature anomalies become significant a few hours later and persist a few hours longer than the salinity anomalies (cf. Fig. 9a). However, like the salinity anomalies, the cool temperatures are surface intensified during the daytime after the rainy day (hours 6–18 in Fig. 9c), as expected in a daytime shallow warm/rain mixing layer. The rain-event-induced temperature anomalies are most extreme ($< -0.16^{\circ}\text{C}$ relative to a previous diurnal cycle at 1 m) during the afternoon following the rainy day (i.e., hours 12–18 in Fig. 9c). And, the anomalies are mixed vertically and become more uniform over the top 25 m during the night after the rainy day (hours 18–30). The distributions of 24-h-mean temperature anomalies at 1 and 5 m

during and after rainy days (0–24 h) span roughly -0.4° to $+0.2^{\circ}\text{C}$ and are very similar to the analogous salinity distributions (Figs. 10a,b).

A back-of-the-envelope calculation shows that these composite cool upper-ocean temperature anomalies due to the rain events are consistent with the heat flux anomalies (dominated by reductions in shortwave radiation) that occur in conjunction with the rain (see Figs. 5 and 6 and section 3b). In particular, a temperature anomaly of -0.1°C over a 10-m surface warm/rain layer is equivalent to a depth-integrated buoyancy anomaly of about $-0.003 \text{ m}^2 \text{ s}^{-2}$. Time-integrating the composite and smoothed B_{net}^T anomaly in Fig. 6, which is about $-2.5 \times 10^{-8} \text{ m}^2 \text{ s}^{-3}$ on average over 36 h (see Fig. 6), yields the same $-0.003 \text{ m}^2 \text{ s}^{-2}$ depth-integrated buoyancy anomaly. It may be noted that these buoyancy anomalies are about half the magnitude and opposite in sign to those associated with salinity. That is, heat flux and temperature anomalies during rainy days are significant to the ocean boundary layer buoyancy response to a rainy day (see also Fig. 9d).

Finally, because cool temperature anomalies in Fig. 9c are strongest during the daytime, it may be noted that the amplitude of the composite diurnal cycle in temperature at 1 m is about 50% weaker during and just after the rain compared to

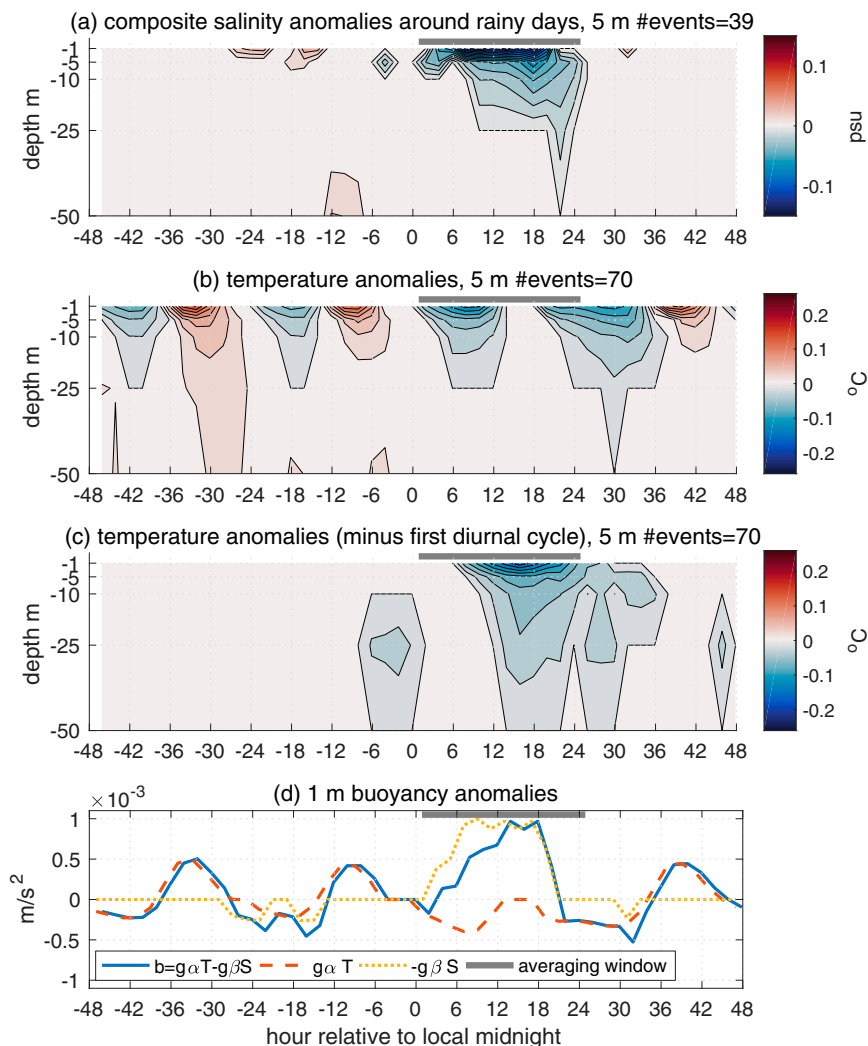


FIG. 9. Composite time series reveal the high-frequency ocean response to a rainy day as observed in the TAO mooring data at 0° , 170°W , including anomalies in (a) salinity; (b),(c) temperature; and (d) buoyancy, which is further decomposed into contributions from temperature and salinity ($b = g\alpha T - g\beta S$). Measured depths are indicated by grid lines in the y axis in (a)–(c); results in (d) are from the sensors at 1 m. Contour spacings are 0.01 psu and 0.02°C . The time listed on the x axes is relative to a zero at local midnight during the rainy day (about 1100 UTC). A 4-day moving average is subtracted from all the variables and at each depth to extract these high-frequency signals. In (c), the data from the first 24 h is also subtracted from all four 24-h periods in order to illustrate the high-frequency deviations from the regular diurnal cycle due to the rain event. The gray bars on the top axes indicate the 24-h averaging window used in Fig. 10, which is lagged 12 h behind the window used to identify the rain events and average the atmospheric anomalies in Fig. 5. The number of events with data from the salinity and temperature sensors at 5 m are given in the panel titles.

before (Fig. 9b; see also Fig. 9d). On the other hand, the peak-to-trough amplitude of the high-frequency buoyancy anomaly at 1 m, which reflects the time-integrated effects of both the salinity and temperature anomalies, is actually somewhat larger than the diurnal cycle before the rain in addition to being shifted up to higher values (Fig. 9d). This strong positive buoyancy anomaly on a daily time scale at 1 m reflects not only the increased buoyancy input to the upper ocean, but

also the increased buoyancy stratification in conjunction with a shallower daytime rain/warm mixing layer.

3) VELOCITY

High-frequency ocean velocity anomalies are modified by and influence (via their effect on mixing) the upper-ocean temperature and salinity stratification. However, velocity observations

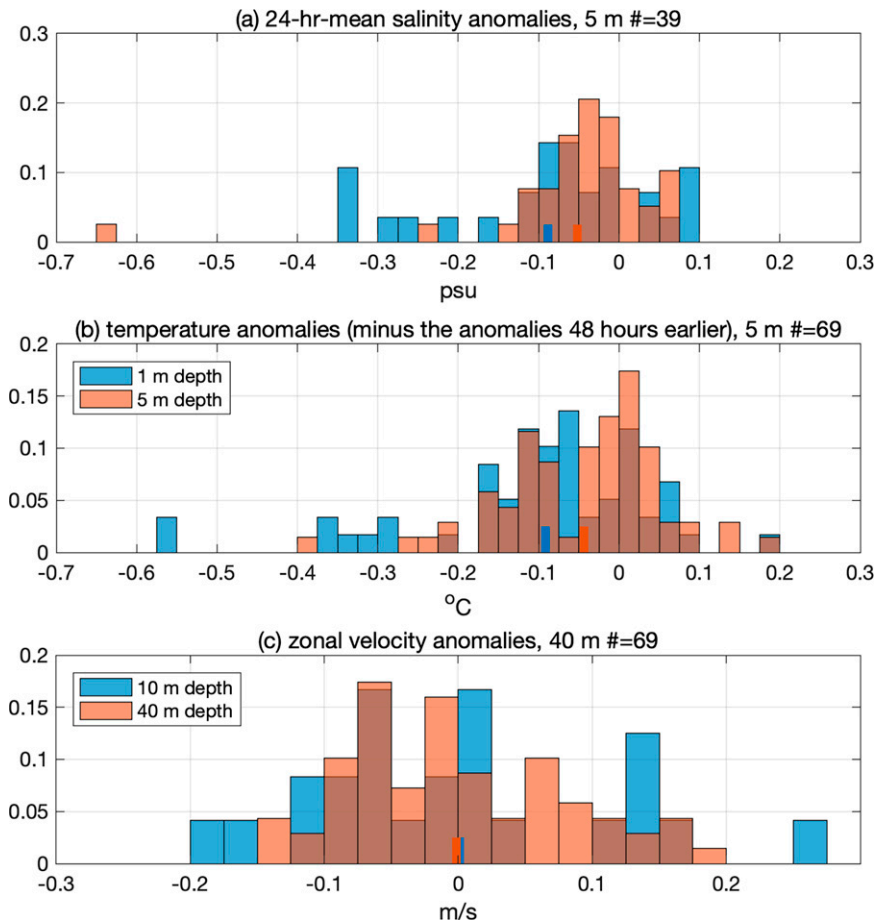


FIG. 10. Distributions of all 24-h-mean upper-ocean (a) salinity, (b) temperature, and (c) zonal velocity anomalies during rain events in the TAO observations at 0° , 170°W . The blue and red distributions show two depths, as indicated in the legends. Means of each distribution are indicated by tick marks on the x axis. The averaging window, which is indicated by the gray bars on the top axes in Fig. 9, is lagged by 12 h relative to the atmospheric averaging window used in Fig. 5, since the strongest ocean anomalies tend to lag the atmospheric forcing.

are unfortunately unavailable at the 1- and 5-m depths where the temperature and salinity anomalies are most prominent. Moreover, the velocity variability below 10 m due to other processes, including the daily variability shown in Fig. 10c as well as higher-frequency variability (not shown), is quite substantial compared to the diurnal signal due to surface forcing. Presumably as a result, no significant rain-event composite zonal velocity anomalies were found. In addition, the diurnal cycle could not be separated from the other variability during and around the rainy days. Below 30 m, some significant diurnal and semidiurnal signals are found before and after the rain event, but these signals are quite sensitive to whether an estimate of the barotropic velocity is removed and are therefore thought to be unrelated to the rain event and thus not shown.

For reference when considering the example events in sections 4 and 5, Masich et al. (2021) find a significant diurnal cycle in the downwind velocity (typically, more negative zonal velocities in this case) from 10- to 50-m depth at 155°W and from 10 to 25 m at 180° using enhanced velocity measurement techniques and

many more diurnal cycles aggregated without regard to rain. The peak-to-trough diurnal amplitude is about 6 and 12 cm s^{-1} at 10-m depth at 155°W and 180° , respectively. The amplitude decays somewhat at deeper depths, but much more rapidly at 180° than 155°W . Masich et al. (2021) also find that diurnal velocity and temperature anomalies are approximately but not exactly in phase, and positive temperature anomalies are associated with more downwind (i.e., more negative zonal) velocities.

4. LES of the ocean surface boundary layer during rainy days

The LES provide valuable insight into the unobserved modulation of strong equatorial shear, stratification, and turbulence by a rain event on the equator in the central Pacific. Specifically, the LES provide highly resolved (0.5 m) vertical profiles of the horizontally averaged temperature, salinity, velocity, vertical shear, density stratification, gradient Richardson number, and turbulent statistics (Figs. 11–13). The turbulent statistics reported below

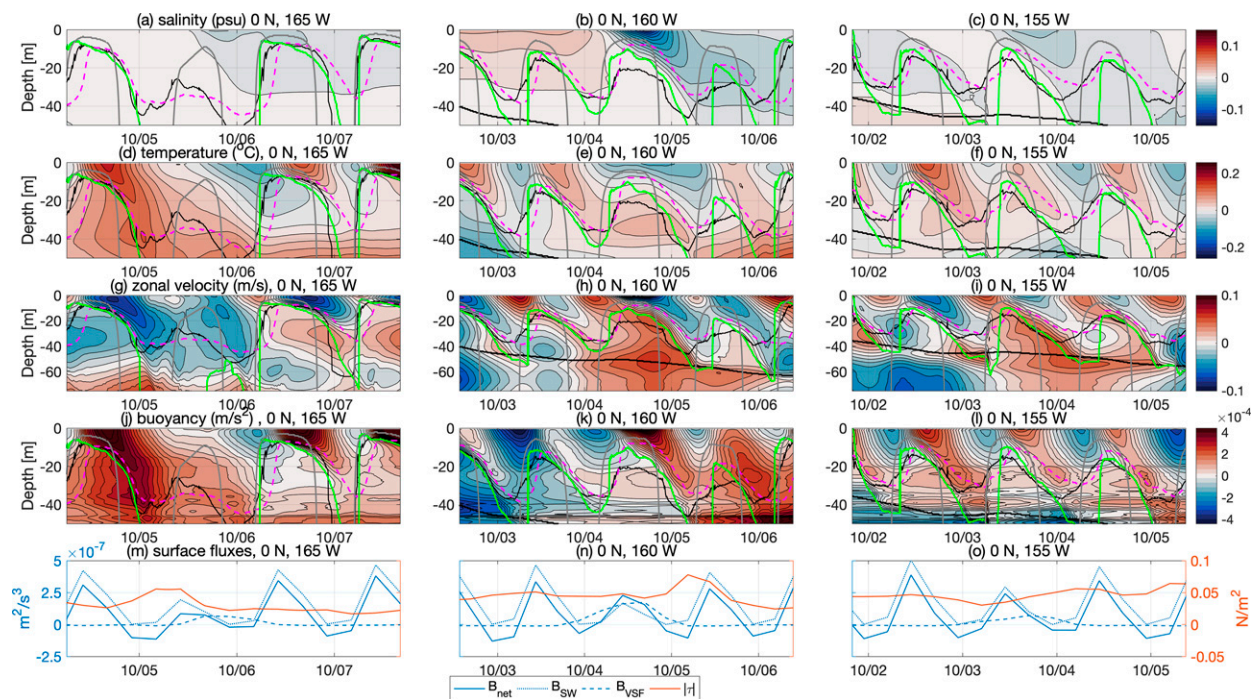


FIG. 11. The high-frequency ocean response to a rainy day in the LES from 165° to 155°W (left to right) is expressed in the anomalies from 4-day mean profiles, including (a)–(c) salinity, (d)–(f) temperature, (g)–(i) zonal velocity, and (j)–(l) buoyancy. (m)–(o) Time series of the total surface fluxes of buoyancy and momentum. Overlaid in (a)–(l) are the mixed layer depth (magenta dashed), the depth H_{Rib} where the bulk Richardson number $Ri_b = 0.2$ (black), the mixing layer depth (green, above which the dissipation $\epsilon > 2 \times 10^{-8} \text{ m}^2 \text{ s}^{-3}$), and the Monin–Obukhov depth (gray). The net surface buoyancy flux in (m)–(o) is further decomposed into shortwave (SW) and virtual-salt flux (VSF) contributions, as indicated in the legend below. Contours are spaced every 0.01 psu, 0.02°C, 0.01 m s^{-1} , and every $0.01 \text{ g}\alpha = 2.9 \times 10^{-5} \text{ m s}^{-2}$ (from top to bottom). Time tick marks are at local midnight.

include the dissipation rate of turbulent kinetic energy ϵ and the turbulent vertical fluxes of salt F_S , temperature/heat F_T , and buoyancy F_b , in addition to zonal momentum F_U . However, only one rain event is simulated at three different locations and times. Moreover, of the three, only one simulation (at 160°W) experiences rainfall exceeding the threshold of a rainy day used in the observational analysis above, i.e., more than 24 mm rain in a single day (0000–2400 UTC) (Fig. 1). The maximum daily rainfall at 155°W and at 165°W is about 14 and 18 mm day^{-1} , respectively (Fig. 1). Nevertheless, these examples are useful for providing insight into the diversity of responses and the sensitivity of the responses to the particular rain-rate threshold of 24 mm chosen above.

The mesoscale ocean context for the three LES is shown in Fig. 2. The shear is strong in the upper 100 m and the stratification is sufficiently weak that the gradient Richardson number $Ri_g < 1$ is low in the upper ocean at all longitudes (see also Fig. 8). However, there is also mesoscale variability between the three LES locations, in addition to variations in the timing and intensity of the rain (Fig. 1). In particular, although there is quite a bit of similarity between the LES mean profiles of temperature and zonal velocity, fairly subtle variations in shear and stratification lead to significant zonal variations in Ri_g . For example, the contour where $Ri_g = 0.5$ (in Fig. 2c) is at about 90 m at 165°W but only 45 m at 160°

and 155°W. These variations significantly impact the parameterized boundary layer turbulence in the regional ocean model, in which boundary layer mixing extends to a depth H_{Rib} (denoted by a black line in Fig. 2c) where a bulk Richardson number

$$Ri_b(H_{Rib}) = \frac{H_{Rib} \Delta b}{|\Delta \mathbf{u}_h|^2 + v_t^2} \quad (4)$$

exceeds a threshold (0.3 in this model); Δb is the buoyancy difference between the depth H_{Rib} and the surface layer (averaged above $0.1 H_{Rib}$), $|\Delta \mathbf{u}_h|^2$ is the squared difference in horizontal velocity between H_{Rib} and the surface layer, and v_t is a turbulent velocity scale that depends on the surface forcing (for more details, see Large et al. 1994). In particular, it may be noted that the depth H_{Rib} (black line in Fig. 2c) varies from about 10 to 45 m between 150° and 170°W along the equator and sometimes deviates quite significantly from the mixed layer depth (magenta dashes in Fig. 2c). We will see that these mesoscale variations in the shear, stratification, and Richardson number influence the turbulence physics simulated in the three LES.

Indeed, perhaps the most notable characteristic of the ocean's response to a rainy day in the LES is the substantial diversity of ocean responses to rain. Nevertheless, a rainy day

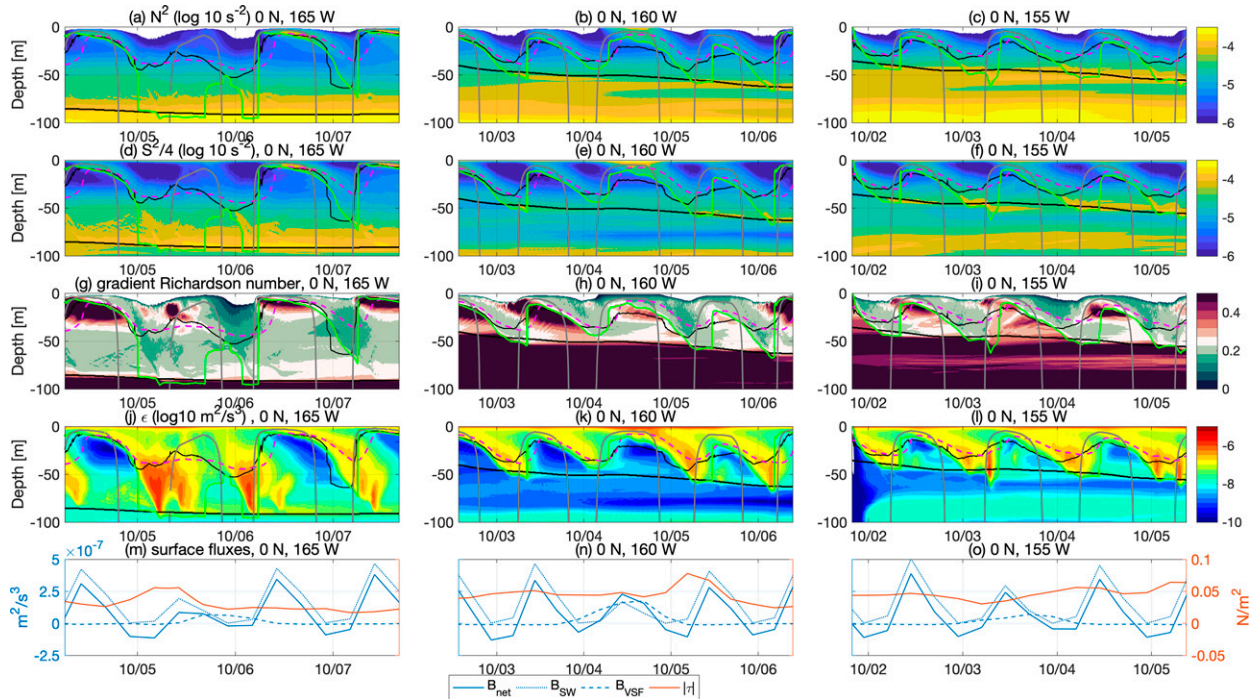


FIG. 12. As in Fig. 11, but the variables shown in the top four rows include (a)–(c) vertical buoyancy gradient N^2 , (d)–(f) the squared vertical shear S^2 (divided by 4 to facilitate comparison with N^2), (g)–(i) the gradient Richardson number $Ri_g = N^2/S^2$, and (j)–(l) the dissipation rate of turbulent kinetic energy ϵ .

does still manifest in some consistent ways in the upper ocean in these simulations. And, both the diversity and consistency are qualitatively similar to observations (Figs. 9 and 10).

For some examples of consistency, observe that at all three longitudes there is a clear reduction in upper-ocean salinity due to the rain, and the diurnal cycles of both the shortwave radiation and the net surface buoyancy flux are suppressed (Fig. 11). In addition, the upper 10 m in the simulation at 160°W is forced by a much stronger freshwater flux anomaly and (as expected) is associated with fresher upper-ocean salinity anomalies and cooler upper-ocean temperature anomalies in the late afternoon when the mixing layer is shallow during the rainy day (Fig. 11). There are also strong upper-ocean buoyancy and buoyancy gradient N^2 anomalies in the upper 10 m at 160°W in the late afternoon (Fig. 12), and these buoyancy anomalies are caused by the surface-intensified reduction of salinity in a shallow daytime mixing layer, consistent with observations.

Although we do not have the observations to compare with many other outputs of the LES, many of these outputs are qualitatively as expected based on analogies to observations in other locations or to more well-observed physics in the central equatorial Pacific (e.g., rain layers to diurnal warm layers). For example, the simulated rain event is associated with upward turbulent salinity fluxes (i.e., downward turbulent buoyancy fluxes) at all longitudes, which seem to vary with the amount of rainfall, the salinity stratification, and the vertical extent of the mixing layer (Fig. 13). In addition, the stronger rain event at 160°W is associated with a more

negative surface zonal velocity anomaly and stronger shear in the afternoon during and after the rain compared to the simulations at other longitudes that are forced by less rain (Figs. 11 and 12). This enhanced velocity and shear anomaly is consistent with the convergence of momentum in an unusually shallow daytime mixing layer due to enhanced B_{net} and stratification (Anderson et al. 1996; Shcherbina et al. 2019). Throughout this stratified daytime rain layer at 160°W, the gradient Richardson number $Ri_g < 1/4$ (Fig. 12h), and the base of the mixing layer is similar to the depth where $Ri_g = 1/4$. The base of this mixing layer happens to be deeper than the mixed layer but shallower than the depth H_{Rib} where the bulk Richardson number $Ri_b = 0.2$ (note that this threshold is different from the one used in the regional ocean model and in Fig. 2, where it is $Ri_b = 0.3$). In addition, this daytime shallow rain layer begins to descend downward in the afternoon when B_{net} is stabilizing, consistent with the mean-profile stability argument that the mixing layer descends as the mean shear overwhelms the mean stratification as in the descent of the daytime warm layer in the central equatorial Pacific (e.g., Schudlich and Price 1992; Smyth et al. 2013; Pham et al. 2017). Finally, the dissipation rate is elevated relative to the other days (Fig. 12) in the shallow rain layer at 160°W, including during its descent to the nighttime deep cycle, as expected when the momentum flux converges across a thinner more strongly sheared mixing layer during daytime (e.g., ten Doeschate et al. 2019; Iyer and Drushka 2021b) (see also studies of diurnal warm layers, e.g., Sutherland et al. 2016; Hughes et al. 2021).

On the other hand, many of the expected or consistent characteristics of the ocean response to the strong rain at

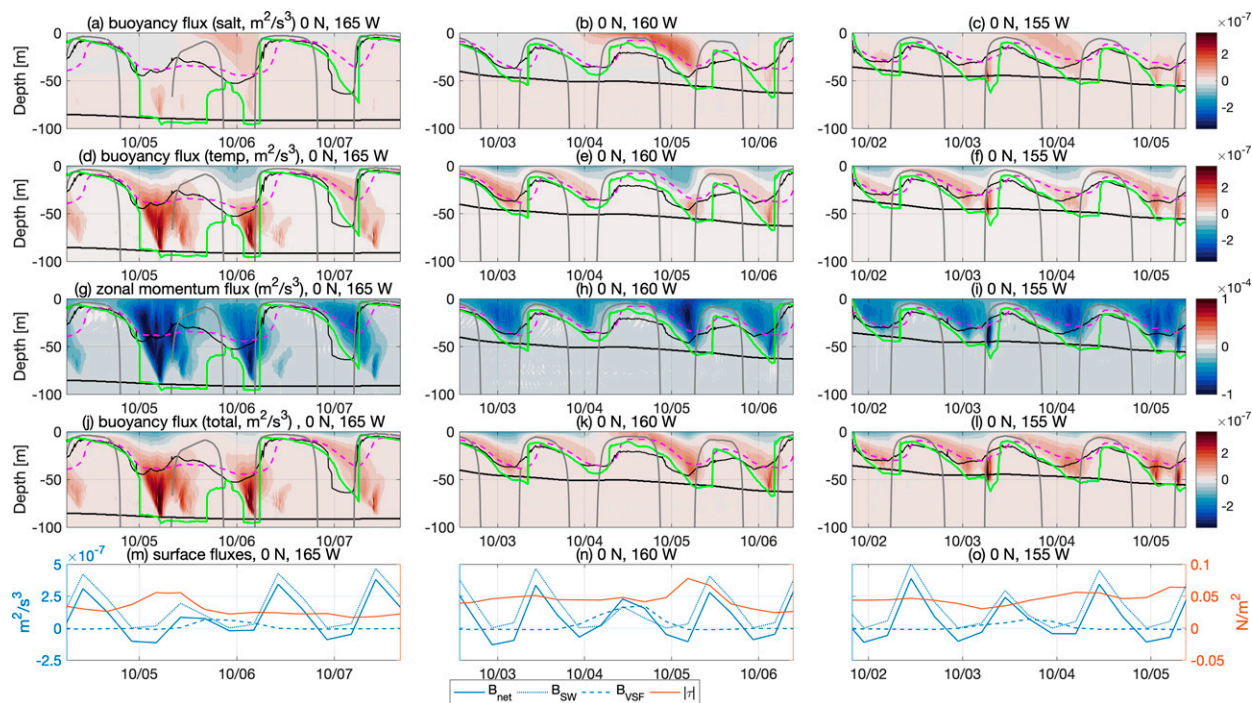


FIG. 13. As in Fig. 11, but the variables in the top four rows include (a)–(c) the downward turbulent salt flux F_S (expressed as a downward buoyancy flux $-g\beta F_S$), (d)–(f) the downward turbulent temperature flux F_T (expressed as a downward buoyancy flux $g\alpha F_T$), (g)–(i) the downward turbulent zonal momentum flux F_U , and (j)–(l) the downward turbulent buoyancy flux $F_b = g\alpha F_T - g\beta F_S$. For reference, the buoyancy fluxes can be converted to equivalent heat fluxes by multiplying by $\rho c_p / (g\alpha) \approx 1.4 \times 10^9 \text{ W m}^{-2} (\text{m}^2 \text{ s}^{-3})^{-1}$.

160°W in LES (as described above) are not even qualitative characteristics of the ocean response to the weaker rain events at 155° and 165°W. In addition, the quantitative nature of even the consistent simulated responses to the rain as well as many other features are complicated by factors other than the rain. For example, consider the question of what controls the magnitude of the salinity response to rain at 1 m? Although more rain will yield more negative salinity anomalies if the salinity is mixed vertically to a similar depth, the LES results highlight how the complexities of ocean mixing complicate the relationship between rainfall and salinity anomalies at 1 m. In quantitative terms, the most negative salinity anomalies at 1 m vary by about a factor of 7 from -0.026 psu at 155°W to -0.12 psu at 160°W to -0.018 psu at 165°W. In comparison, the total-event rainfall differs similarly but by a much smaller factor of about 2.5, from 17.7 mm at 155°W, to 43 mm at 160°W, to 19.2 mm at 165°W. Notably, the relationship between the salinity anomaly at 1 m and the rainfall is neither monotonic nor a linear function of the total rain (cf. Drushka et al. 2016; ten Doeschate et al. 2019). In addition, this nonlinearity would be exaggerated by accounting for the wind stress or wind speed, which is expected to be in some sense inversely related to the salinity anomaly and perhaps linearly so if the mixing layer depth is proportional to wind speed (e.g., Pollard et al. 1973; Drushka et al. 2016), but not necessarily if, e.g., the mixing layer depth scales as wind speed to the third power as in Monin–Obukhov similarity theory (Monin and Obukhov 1954) or another model (for some

models of wind-driven mixed layer deepening; see, e.g., Kato and Phillips 1969; Price 1979; Trowbridge 1992; Pham and Sarkar 2017). In the LES, the weakest salinity anomaly at 1 m and the deepest mixing layers during and after the rain occur at 165°W in conjunction with the weakest wind (Figs. 11m–o). In contrast, under a fairly similar rain rate and stronger wind, a shallow daytime warm/rain layer does emerge at 155°W as it does at 160°W under much stronger rain and stronger wind.

The somewhat surprisingly weak 1-m salinity anomaly at 165°W reflects a broader set of different characteristics in that simulation relative to the other two. First, there is a particularly thick, deep, and highly sheared but marginally unstable layer with $Ri_g \approx 1/4$ and vigorous deep-cycle turbulence that can be sustained by shear through even stabilizing daytime B_{net} (Figs. 12 and 13). Although the thickness and depth of the deep cycle seems unique at 165°W among these three LES, we expect a thick deep cycle to be fairly common in the central equatorial Pacific, albeit modulated by mesoscale variability [e.g., based on observations at 140°W and the modeling of Pei et al. (2020), Cherian et al. (2021), and Whitt et al. (2022)]. Second, the diurnal cycle in B_{net} is especially depressed by the rain event at 165°W due to the timing of the stabilizing rain at night and the relatively strong suppression of downwelling shortwave radiation during the day. In contrast, the rain peaks at about midday at 160°W, such that the rain does not suppress convection at night and maintains a relatively strong stabilizing B_{net} during the day. As a consequence, the diurnal cycle in buoyancy is more strongly

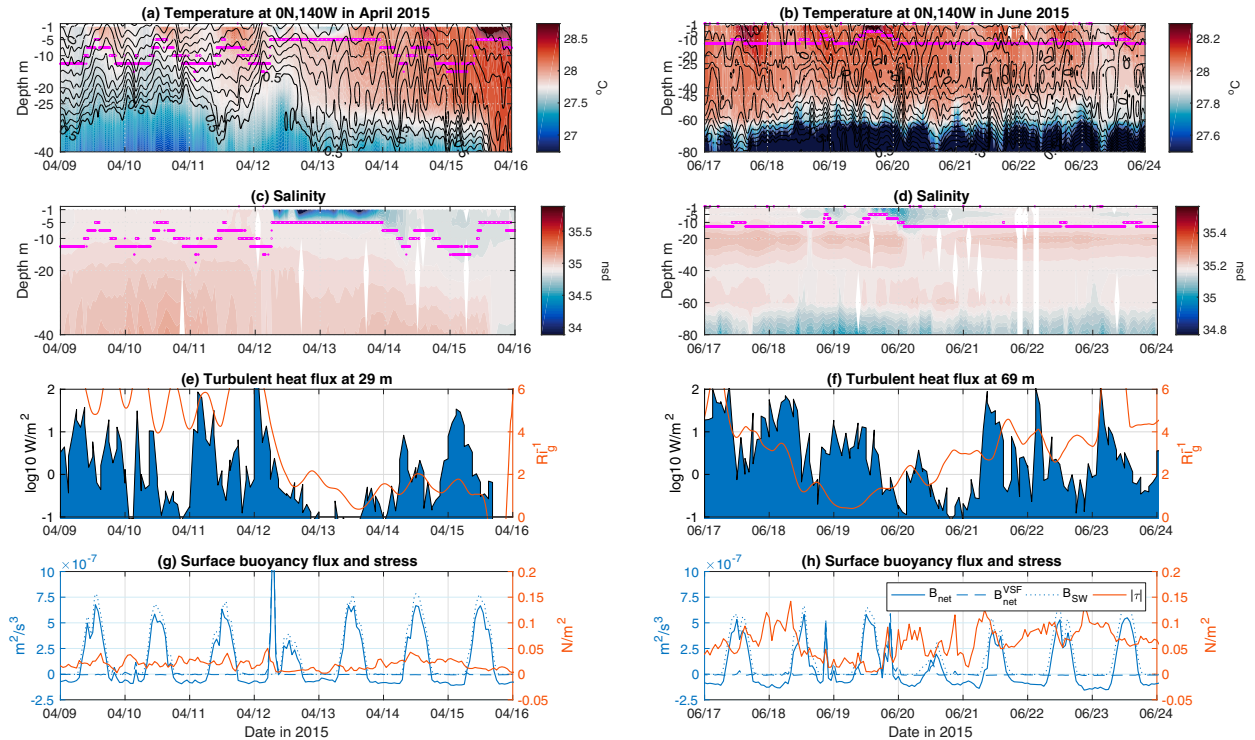


FIG. 14. Observations of two rain events in the TAO data at 0° , 140°W are presented: (a),(b) temperature (color), zonal velocity (black contours ever 0.05 m s^{-1}), and mixed layer depth (magenta); (c),(d) salinity and mixed layer depth; (e),(f) the downward turbulent heat flux (blue area) and the gradient Richardson number Ri_g (red line, smoothed with a 6-h moving average in time); (g),(h) the surface stress (red) and the net surface buoyancy flux (blue), the latter of which is decomposed into a shortwave-only contribution (smoothed to 1-h resolution with a moving average, dotted), and a freshwater/salinity contribution (VSF; dashed). Time tick marks are at local midnight. Note the different y axis and color bar ranges in (a)–(d).

disrupted by the weaker rain event at 165°W than the stronger rain event at 160°W .

In summary, the LES results provide limited qualitative support for the idea espoused in the introduction, that rains less than 24 mm day^{-1} typically have a fairly modest direct impact on the boundary layer buoyancy (via salinity) and hence physics. However, these results also underscore the observational result that rain events are also associated with systematic heat flux anomalies that can (on their own) alter the upper-ocean buoyancy enough to rather dramatically alter the ocean boundary layer physics, e.g., by preventing the formation of the shallow daytime warm/rain layer in the example at 165°W . Moreover, the heat flux anomalies and hence the impacts on the ocean physics are not necessarily linearly related to rain rates.

5. Does a rain event modify the turbulent heat and buoyancy fluxes in the deep cycle?

Although it is clear from the results of the previous sections that rainy days significantly modify the turbulence in the upper 10–20 m of the ocean boundary layer in the central equatorial Pacific, it is not so clear from those results how the rain modulates the fluxes of heat and buoyancy in the deep-cycle turbulence below the mixed layer, which is a major reason

why equatorial turbulence has a potent effect on the sea surface temperature and climate (e.g., Moum et al. 2013). This section uses the LES results to address the question of whether the rain affects the deep-cycle turbulence in the central equatorial Pacific. However, the section begins with some motivating observations.

a. Observations from χ pods on the TAO mooring at 0° , 140°W

Remarkably, given how rare rainy days are at 0° , 140°W (Fig. 3), there are observations from χ pods on the TAO mooring of the ocean's turbulent response to two rainy days during the 2015 El Niño at 0° , 140°W (Fig. 14). As in the examples from LES discussed in the previous section, the rain is associated with negative salinity anomalies in the top 10 m that persist for about 1–2 days. Shortwave radiation is substantially reduced, the diurnal warming of the sea surface temperature is depressed, and the mixed layer is anomalously shallow for a period of time. Below the mixed layer, the turbulent heat flux weakens during both rain events. Consistent with reduced turbulence, the gradient Richardson number increases from $Ri_g \approx 0.25$ indicative of marginal instability to $Ri_g \approx 1$ indicative of stability. Although just two examples with data from only a single depth below the mixed layer, these results raise the intriguing suggestion that the surface

buoyancy forcing due to the rain and solar radiation anomalies might disrupt the balance between shear and stratification as well as the deep-cycle turbulence in the marginally unstable layer below the surface mixed layer.

b. LES

To quantitatively evaluate how deep-cycle turbulence is influenced by the rain, we use the LES results and follow Whitt et al. (2022) by quantifying the maximum over depth of the daily-averaged turbulent temperature flux $\langle F_T \rangle^{\max}$ and buoyancy flux $\langle F_b \rangle^{\max}$. Whitt et al. (2022) focus on this maximum for two reasons: First, this subsurface maximum flux bounds the maximum effect of mixing in a daily-averaged and depth-integrated upper-ocean heat or buoyancy budget. Second, the maximum flux, and the depth where it occurs z_{\max} , can be used together with an estimate of the surface flux and an estimate of the depth of the surface mixing layer, where the flux approximately goes to zero, to constrain a simple model of the whole upper-ocean heat or buoyancy flux profile.

Whitt et al. (2022) focus first on the buoyancy flux $\langle F_b \rangle^{\max}$ because of its role as a sink in the turbulent kinetic energy budget, which is approximately in the canonical production–buoyancy flux–dissipation balance (Osborn 1980), and because it was hypothesized that heat fluxes are approximately proportional to buoyancy fluxes in the equatorial Pacific. Furthermore, it was hypothesized that $\langle F_b \rangle^{\max}$ can be scaled as a power law product including two physical factors that nominally represent the turbulent momentum flux and mean shear, based on an approximate proportionality between shear production and buoyancy flux in the turbulent kinetic energy budget in the deep cycle [with a canonical proportionality coefficient of about 0.2 (Gregg et al. 2018)]. The first and most important factor in the power law is the bulk vertical shear S_b , which is defined from a linear fit to the velocity averaged over a day from the base of the low- Ri_g deep-cycle layer ($Ri_g < 0.35$; thick black lines in Figs. 11–13) to 5 m depth. The second is the friction velocity $u_* = \sqrt{|\tau|/\rho_{sw}}$, where $|\tau|$ is the magnitude of the wind stress. Smyth et al. (2021) recently found that the mean shear and the wind stress were the most useful predictors of the intensity of deep-cycle turbulence in years of χ pod observations at 0° , 140° W. And, Whitt et al. (2022) show that power laws of the form

$$\langle F_b \rangle^{\max} = 3.1 \times 10^{-6} |S_b|^{0.88}, \quad \text{and} \quad (5)$$

$$\langle F_b \rangle^{\max} = 0.16 u_*^{2.05} |S_b|^{0.98}, \quad (6)$$

(optimized via linear regression on the LES output) explain about 70% and 90% of the simulated variance in $\langle F_b \rangle^{\max}$ in 68 days of LES (34 at each of 0° and 3° N along 140° W). In addition, these scalings explain about 50% and 40%, respectively, of the observed variance in $\langle F_b \rangle^{\max}$ with mean bias less than a factor of 2 in a completely independent validation on 38 days of observations with microstructure profiles about every 10 min at 0° , 140° W from Lien et al. (1995). Finally, the resulting scalings are derived empirically via linear regression,

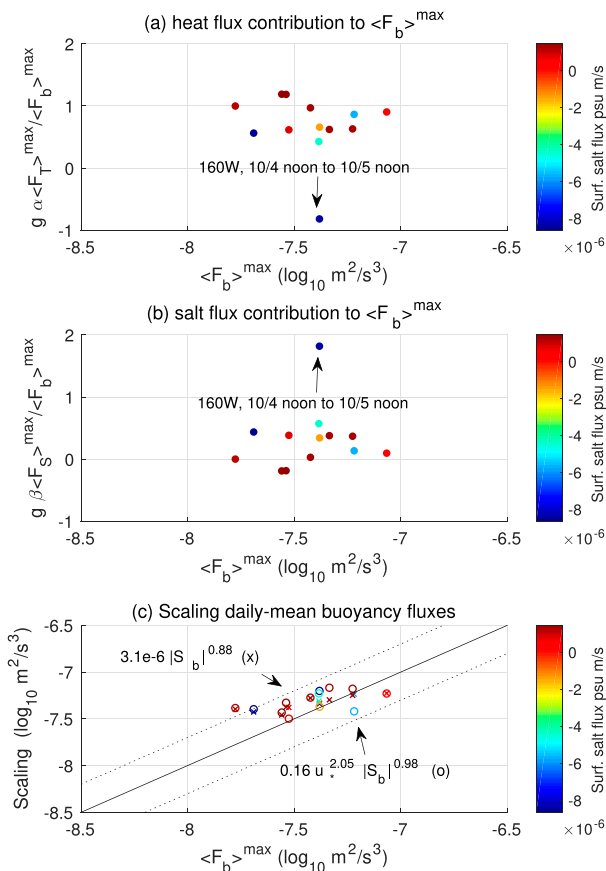


FIG. 15. (a)–(c) Scatterplots show several properties of the maximum over depth of the daily-mean downward turbulent buoyancy flux $\langle F_b \rangle^{\max}$ in the three LES. These daily means begin and end at about noon local time (2230 UTC), for consistency with Whitt et al. (2022). The contributions of the turbulent temperature and salt fluxes to $\langle F_b \rangle^{\max}$ are shown in (a),(b) and two scalings (5) and (6) are shown in (c). The net virtual surface salt flux at the surface is shown in color (rainy days are blue). The most rainy day at 160° W is anomalous in (a) and (b) and pointed out with an arrow.

but the approximate form $\langle F_b \rangle^{\max} \approx 0.2 u_*^2 S_b$ can also be derived theoretically (Smyth et al. 2017, 2021).

A hypothesis that one might derive from these results is that the surface buoyancy flux has little significant and direct influence on or predictive power over $\langle F_b \rangle^{\max}$ or the energetics of the deep-cycle turbulence. Here, we test this hypothesis in the extreme case of strong positive surface buoyancy flux anomalies associated with a rare heavy rain event in the central Pacific using the three LES reported above.

Perhaps surprisingly in light of what seemed like quite substantial deviations in the near-surface physics due to rain, not a single daily $\langle F_b \rangle^{\max}$ deviates from either scaling by more than about a factor of 2 across all three rain events [Fig. 15c shows results from 13 full days, each of which starts and ends at 2230 UTC or about noon local time for consistency with Whitt et al. (2022)]. To the extent there are outliers in $\langle F_b \rangle^{\max}$, they do not include the days with the heaviest rain. Furthermore, $\langle F_b \rangle^{\max}$ does not seem to be systematically lower

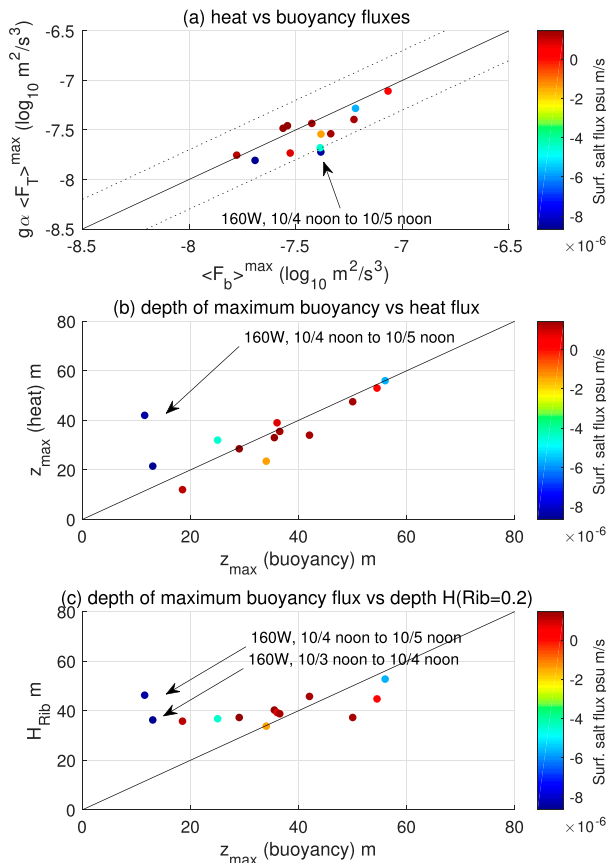


FIG. 16. Scatterplots show the relationship between the maximum over depth of the daily-mean turbulent buoyancy flux $\langle F_b \rangle^{\max}$ and the maximum over depth of the daily-mean turbulent temperature flux $\langle F_T \rangle^{\max}$. (a) An approximate linear relationship is shown between $\langle F_T \rangle^{\max}$ and $\langle F_b \rangle^{\max}$, and the buoyancy-scaled temperature flux $g\alpha\langle F_T \rangle^{\max}$ is within a factor of two of $\langle F_b \rangle^{\max}$ although $\langle F_b \rangle^{\max}$ is typically slightly stronger than $g\alpha\langle F_T \rangle^{\max}$. (b) A close relationship is also shown between the depths z_{\max} where the respective maxima $\langle F_T \rangle^{\max}$ and $\langle F_b \rangle^{\max}$ occur, with one notable exception on the rainiest day noted by an arrow. (c) The depth H_{Rib} where the bulk Richardson number $\text{Ri}_b = 0.2$ is related to z_{\max} , with two notable exceptions that seem to be associated with the rain events and are noted by arrows.

or higher on rainy days, when it takes both relatively high ($7 \times 10^{-8} \text{ m}^2 \text{ s}^{-3}$) and low ($3 \times 10^{-8} \text{ m}^2 \text{ s}^{-3}$) values. The buoyancy perturbation due to rain also has no obvious impact on the depth of the deep-cycle layer defined by low $\text{Ri}_g < 0.35$ (thick black lines in Figs. 11–13). And, the maximum daily-mean downward turbulent temperature flux $\langle F_T \rangle^{\max}$ (or equivalently heat flux) can be predicted within a factor of 2 from $\langle F_b \rangle^{\max}$ on all 13 full days from the three events (Fig. 16a). Taken together, these results support the hypothesis that even relatively rainy days have little impact on the deep-cycle turbulence in the central equatorial Pacific.

However, there are also some more subtle indications that rain does have some impact on the deep-cycle turbulence. Notably, on the rainiest day at 160°W (the bluest dot), the

depths at which the maximum heat and buoyancy flux occur differ dramatically. The maximum heat flux occurs at about 40 m, whereas the maximum buoyancy flux occurs at about 15 m (Fig. 16b). In addition, at the depth z_{\max} where $\langle F_b \rangle^{\max}$ occurs, the temperature flux is actually reversed (so heat is transported upward) and the upward salinity flux sets $\langle F_b \rangle^{\max}$ (Figs. 15a,b). On the other hand, with the exception of this one rainy day, i.e., the only simulated day in which the rain exceeds our 24-mm threshold, the maximum occurs at a fairly similar depth z_{\max} in both the $\langle F_T \rangle$ and $\langle F_b \rangle$ profiles (Fig. 16b), and the heat flux generally dominates $\langle F_b \rangle^{\max}$ (Figs. 15a,b). A final comment can be made with regard to the depth z_{\max} . Although z_{\max} can often be predicted from the daily maximum depth where the bulk Richardson number is 0.2 (as in Whitt et al. 2022), there are two days where H_{Rib} and z_{\max} differ notably in these LES (Fig. 16c). The most extreme failure of the $H_{\text{Rib}} \sim z_{\max}$ scaling (with $z_{\max} < H_{\text{Rib}}$) occurs at the end of the rainy day at 160°W, and the failure is likely caused by the relatively strong, shallow, and long-lived upward turbulent salinity and downward turbulent buoyancy flux anomalies that are required to erode the buoyant warm/rain layer (Figs. 11b,k and 13b,k). Taken together with the observational examples, these results suggest that surface buoyancy fluxes can significantly modify the deep-cycle dynamics: by modifying the partitioning of buoyancy fluxes between heat and salinity as well as systematically reducing the vertical penetration and modifying the vertical structure of the turbulent fluxes of heat and buoyancy.

6. Conclusions

The coincidental simulation of the ocean response to a rare rainy day in large-eddy simulations in the central equatorial Pacific raised the question: how does rainfall modify the air–sea buoyancy exchange and the unique ocean surface boundary layer physics, and in particular the deep-cycle turbulence, on the equator in the central Pacific?

An analysis of atmospheric surface observations and reanalysis demonstrates that rainy days > 24 mm, in which the buoyancy due to the rain substantially modifies the fairly regular diurnal cycle of upper-ocean buoyancy and physics, are rare. Such rainy days occur roughly once every 100 days on average in the central equatorial Pacific but are more common during boreal winter and El Niño. Composites of atmospheric surface conditions quantify a variety of systematic changes in the surface atmosphere during a rainy day. Most importantly, they highlight fairly dramatic reductions in the daytime downwelling shortwave radiation, which is crucial to account for when assessing the influence of a rain event on the air–sea buoyancy flux as well as the upper-ocean buoyancy and physics. On average, the reduction in shortwave radiation together with the stabilizing rain yield about a 50% reduction in the amplitude of the diurnal cycle in addition to an overall increase in the net air–sea buoyancy flux during rain events. The significance of these changes for ocean physics is highlighted in a large-eddy simulation in which reduced daytime shortwave radiation during a rain event suppresses

the formation of the typical daytime warm/fresh layer even under stabilizing rain.

An analysis of the observed upper-ocean responses to rainy days highlights the substantial spread in the distributions of the upper-ocean salinity and temperature. The scatter in these oceanic responses is plausibly attributable to the variability in the atmospheric forcing during the rainy days, variability in the oceanic preconditions, or other intrinsic oceanic variability that occurs during the rain event but is unrelated to the rain. Nevertheless, the sustained high-frequency observations from the TAO mooring at 0°, 170°W do reveal significant composite temperature, salinity, and buoyancy responses to a rainy day. These anomalies are surface intensified and strongest (roughly -0.12 psu or $+0.0009$ m s⁻² and -0.16°C or -0.0005 m s⁻² at 1 m on average on days with more than 24 mm of rain) during the daytime during and after a rain event, consistent with a shallow daytime warm/rain mixing layer and the anomalies in the air-sea flux of heat and freshwater during the rain event. Although these composite results reflect significant quantitative relationships between the rain rate and the magnitude of other atmosphere-ocean anomalies, caution is required if extrapolating or predicting based on these relationships due to the substantial variability between rainy days, the large number of relevant variables, and the comparatively limited number of observations.

Three large-eddy simulations provide the first explicit (unparameterized) look at how ocean boundary layer turbulence responds to a rare strong rain event on the equator in the central equatorial Pacific, which would be very difficult to intentionally observe in a temporary process study. On the one hand, the results of the simulation at 160°W, the only run in which the rain was sufficient to meet our threshold of 24 mm for a rainy day, are generally consistent with the observations from the TAO mooring, and many features of the solutions are as expected based on analogies with observations of the ocean response to rain elsewhere. On the other hand, the LES results also highlight how the complexities of the ocean mixing complicate the upper-ocean response to rain, for example, when the shortwave radiation anomaly associated with the rain event prevented the formation of the shallow daytime warm/fresh mixing layer under the rain at 165°W.

The manuscript concludes with the finding that a rainy day can have subtle but significant impacts on the diurnal deep-cycle turbulence, which is most significant for the upper-ocean heat and momentum budgets. In particular, neither the total vertical extent of the deep-cycle layer nor the bulk energetics of the deep-cycle turbulence, which is controlled primarily by the ocean shear and wind stress, are significantly modified during a rainy day in the LES. However, a rainy day can completely change the partitioning of the deep-cycle buoyancy flux between heat and salinity fluxes (even reversing the signs). And, the rain may systematically modify the vertical structure of the turbulent fluxes and lead to relatively stronger fluxes at shallower depths. Consistent with this qualitative conclusion, observed turbulent heat fluxes from moored χ pods below the mixed layer decline during two rare rainy days at 0°, 140°W during the 2015 El Niño.

Finally, future work is needed to leverage and build on these results toward a more complete understanding of how

rain impacts the lower atmosphere and upper ocean. Most importantly, although the results are expected to be of general relevance to rainy days in the central equatorial Pacific, the lower atmosphere and upper ocean responses to a rainy day are expected to differ qualitatively in other locations, where processes that are omitted (e.g., surface waves) and/or of minor importance (e.g., wind) in the central equatorial Pacific are far more significant. Finally, although rainy days that significantly perturb upper-ocean buoyancy dynamics are rare in the central equatorial Pacific, their strong correlation with El Niño and the importance of accurate simulations of El Niño for global long-range weather and climate simulation suggests that further study may be warranted in this particular region and context, as well as more broadly.

Acknowledgments. This paper was written while the author was supported by the research and analysis program of NASA Earth Science (Physical Oceanography and Salinity Science). The software and simulations were originally developed and run by the author at NCAR under NOAA Contract NA18OAR4310408 from the Climate Program Office. High-performance computing support is from Cheyenne (doi:10.5065/D6RX99HX) provided by NCAR's Computational and Information Systems Laboratory, sponsored by the National Science Foundation. We acknowledge the TAO mooring infrastructure and all of the people who sustain it. TAO observational data were made available by the GTMBA Project Office of NOAA/PMEL (<https://www.pmel.noaa.gov/tao/drupal/disdel/>). I acknowledge my colleague John Taylor as the architect and principal developer of the original DIABLO LES model. Ryan Holmes assisted in setting up the regional ocean modelling simulation. And, I acknowledge the broader TPOS pre-field modeling studies teams at NCAR for valuable discussions that helped facilitate this work, including Deepak Cherian, Bill Large, Frank Bryan, Anna-Lena Deppenmeier, Scott Bachman, LuAnne Thompson, Ren-Chieh Lien, and Billy Kessler. Luigi Cavaleri and two anonymous reviewers are thanked for their constructive comments.

Data availability statement. The data are published online, including the TAO/TRITON buoy and mooring data (<https://www.pmel.noaa.gov/tao/drupal/disdel/>), the JRA55do atmospheric surface reanalysis (<https://climate.mri-jma.go.jp/pub/ocean/JRA55-do/>), the COBESST sea-surface temperature analysis (<https://psl.noaa.gov/data/gridded/data.cobe.html>), the ONI (https://origin.cpc.ncep.noaa.gov/products/analysis_monitoring/ensostuff/ONI_v5.php), and the LES output (<http://doi.org/10.6084/m9.figshare.19068164>). Additionally, relevant source code and configuration files (Whitt 2022b) and analysis and visualization software (Whitt 2022a) are also published.

REFERENCES

- Adler, R. F., G. Gu, M. Sapiiano, J.-J. Wang, and G. J. Huffman, 2017: Global precipitation: Means, variations and trends during the satellite era (1979–2014). *Surv. Geophys.*, **38**, 679–699, <https://doi.org/10.1007/s10712-017-9416-4>.

- Allen, M. R., and W. J. Ingram, 2002: Constraints on future changes in climate and the hydrologic cycle. *Nature*, **419**, 228–232, <https://doi.org/10.1038/nature01092>.
- Anderson, J. E., and S. C. Riser, 2014: Near-surface variability of temperature and salinity in the near-tropical ocean: Observations from profiling floats. *J. Geophys. Res. Oceans*, **119**, 7433–7448, <https://doi.org/10.1002/2014JC010112>.
- Anderson, P. S., 2009: Measurement of Prandtl number as a function of Richardson number avoiding self-correlation. *Bound.-Layer Meteor.*, **131**, 345–362, <https://doi.org/10.1007/s10546-009-9376-4>.
- Anderson, S. P., R. A. Weller, and R. B. Lukas, 1996: Surface buoyancy forcing and the mixed layer of the western Pacific warm pool: Observations and 1D model results. *J. Climate*, **9**, 3056–3085, [https://doi.org/10.1175/1520-0442\(1996\)009<3056:SBFATM>2.0.CO;2](https://doi.org/10.1175/1520-0442(1996)009<3056:SBFATM>2.0.CO;2).
- Asher, W. E., A. T. Jessup, R. Branch, and D. Clark, 2014: Observations of rain-induced near-surface salinity anomalies. *J. Geophys. Res. Oceans*, **119**, 5483–5500, <https://doi.org/10.1002/2014JC009954>.
- Babanin, A., 2006: On a wave-induced turbulence and a wave-mixed upper ocean layer. *Geophys. Res. Lett.*, **33**, L20605, <https://doi.org/10.1029/2006GL027308>.
- Balasubramaniam, R., and C. Ruf, 2020: Characterization of rain impact on L-band GNSS-R ocean surface measurements. *Remote Sens. Environ.*, **239**, 111607, <https://doi.org/10.1016/j.rse.2019.111607>.
- Cavaleri, L., and L. Bertotti, 2017: The attenuation of swell waves by rain. *Geophys. Res. Lett.*, **44**, 10504–10510, <https://doi.org/10.1002/2017GL075458>.
- , and —, 2018: Rain on generative seas. *Geophys. Res. Lett.*, **45**, 7049–7056, <https://doi.org/10.1029/2018GL078006>.
- , —, and J.-R. Bidlot, 2015: Waving in the rain. *J. Geophys. Res. Oceans*, **120**, 3248–3260, <https://doi.org/10.1002/2014JC010348>.
- Cherian, D., E. Shroyer, H. Wijesekera, and J. Moum, 2020: The seasonal cycle of upper-ocean mixing at 8°N in the Bay of Bengal. *J. Phys. Oceanogr.*, **50**, 323–342, <https://doi.org/10.1175/JPO-D-19-0114.1>.
- , D. Whitt, R. Holmes, R.-C. Lien, S. Bachman, and W. Large, 2021: Off-equatorial deep-cycle turbulence forced by tropical instability waves in the equatorial Pacific. *J. Phys. Oceanogr.*, **51**, 1575–1593, <https://doi.org/10.1175/JPO-D-20-0229.1>.
- Clayton, C. A., J. B. Edson, A. Paget, R. Graham, and B. Greenwood, 2019: Effects of rainfall on the atmosphere and the ocean during SPURS-2. *Oceanography*, **32**, 86–97, <https://doi.org/10.5670/oceanog.2019.216>.
- Danabasoglu, G., W. G. Large, J. J. Tribbia, P. R. Gent, B. P. Briegleb, and J. C. McWilliams, 2006: Diurnal coupling in the tropical oceans of CCSM3. *J. Climate*, **19**, 2347–2365, <https://doi.org/10.1175/JCLI3739.1>.
- Deppenmeier, A.-L., F. O. Bryan, W. S. Kessler, and L. Thompson, 2021: Modulation of cross-isothermal velocities with ENSO in the tropical Pacific cold tongue. *J. Phys. Oceanogr.*, **51**, 1559–1574, <https://doi.org/10.1175/JPO-D-20-0217.1>.
- DiTullio, G. R., and E. A. Laws, 1991: Impact of an atmospheric-oceanic disturbance on phytoplankton community dynamics in the North Pacific central gyre. *Deep-Sea Res.*, **38A**, 1305–1329, [https://doi.org/10.1016/0198-0149\(91\)90029-F](https://doi.org/10.1016/0198-0149(91)90029-F).
- Drushka, K., S. T. Gille, and J. Sprintall, 2014: The diurnal salinity cycle in the tropics. *J. Geophys. Res. Oceans*, **119**, 5874–5890, <https://doi.org/10.1002/2014JC009924>.
- , W. E. Asher, B. Ward, and K. Walesby, 2016: Understanding the formation and evolution of rain-formed fresh lenses at the ocean surface. *J. Geophys. Res. Oceans*, **121**, 2673–2689, <https://doi.org/10.1002/2015JC011527>.
- , —, A. T. Jessup, E. J. Thompson, S. Iyer, and D. Clark, 2019: Capturing fresh layers with the surface salinity profiler. *Oceanography*, **32**, 76–85, <https://doi.org/10.5670/oceanog.2019.215>.
- Duce, R. A., and N. W. Tindale, 1991: Atmospheric transport of iron and its deposition in the ocean. *Limnol. Oceanogr.*, **36**, 1715–1726, <https://doi.org/10.4319/lo.1991.36.8.1715>.
- Echevarria, E., M. Hemer, and N. Holbrook, 2019: Seasonal variability of the global spectral wind wave climate. *J. Geophys. Res. Oceans*, **124**, 2924–2939, <https://doi.org/10.1029/2018JC014620>.
- Edson, J. B., and Coauthors, 2013: On the exchange of momentum over the open ocean. *J. Phys. Oceanogr.*, **43**, 1589–1610, <https://doi.org/10.1175/JPO-D-12-0173.1>.
- Fairall, C. W., E. F. Bradley, J. Hare, A. A. Grachev, and J. B. Edson, 2003: Bulk parameterization of air-sea fluxes: Updates and verification for the COARE algorithm. *J. Climate*, **16**, 571–591, [https://doi.org/10.1175/1520-0442\(2003\)016<0571:BPOASF>2.0.CO;2](https://doi.org/10.1175/1520-0442(2003)016<0571:BPOASF>2.0.CO;2).
- Fofonoff, N. P., and R. Millard Jr., 1983: Algorithms for computation of fundamental properties of seawater. UNESCO Tech. Paper in Marine Science 44, 58 pp., <http://unesdoc.unesco.org/images/0005/000598/059832eb.pdf>.
- Gregg, M. C., H. Peters, J. Wesson, N. Oakey, and T. Shay, 1985: Intensive measurements of turbulence and shear in the equatorial undercurrent. *Nature*, **318**, 140–144, <https://doi.org/10.1038/318140a0>.
- , E. A. D’Asaro, J. J. Riley, and E. Kunze, 2018: Mixing efficiency in the ocean. *Annu. Rev. Mar. Sci.*, **10**, 443–473, <https://doi.org/10.1146/annurev-marine-121916-063643>.
- Haidvogel, D. B., and Coauthors, 2008: Ocean forecasting in terrain-following coordinates: Formulation and skill assessment of the regional ocean modeling system. *J. Comput. Phys.*, **227**, 3595–3624, <https://doi.org/10.1016/j.jcp.2007.06.016>.
- Hanson, A. K., N. W. Tindale, and M. A. Abdel-Moati, 2001: An equatorial Pacific rain event: Influence on the distribution of iron and hydrogen peroxide in surface waters. *Mar. Chem.*, **75**, 69–88, [https://doi.org/10.1016/S0304-4203\(01\)00027-5](https://doi.org/10.1016/S0304-4203(01)00027-5).
- Ho, D. T., and J. J. Schanze, 2020: Precipitation-induced reduction in surface ocean pCO₂: Observations from the eastern tropical Pacific Ocean. *Geophys. Res. Lett.*, **47**, e2020GL088252, <https://doi.org/10.1029/2020GL088252>.
- Holmes, R. M., J. D. Zika, and M. H. England, 2019a: Diathermal heat transport in a global ocean model. *J. Phys. Oceanogr.*, **49**, 141–161, <https://doi.org/10.1175/JPO-D-18-0098.1>.
- , —, R. Ferrari, A. F. Thompson, E. R. Newsom, and M. H. England, 2019b: Atlantic Ocean heat transport enabled by Indo-Pacific heat uptake and mixing. *Geophys. Res. Lett.*, **46**, 13 939–13 949, <https://doi.org/10.1029/2019GL085160>.
- Huang, B., and Coauthors, 2017: Extended Reconstructed Sea Surface Temperature, version 5 (ERSSTv5): Upgrades, validations, and intercomparisons. *J. Climate*, **30**, 8179–8205, <https://doi.org/10.1175/JCLI-D-16-0836.1>.
- Hughes, K. G., J. N. Moum, E. L. Shroyer, and W. D. Smyth, 2021: Stratified shear instabilities in diurnal warm layers. *J. Phys. Oceanogr.*, **51**, 2583–2598, <https://doi.org/10.1175/JPO-D-20-0300.1>.
- Ishii, M., A. Shouji, S. Sugimoto, and T. Matsumoto, 2005: Objective analyses of sea-surface temperature and marine meteorological

- variables for the 20th century using ICOADS and the Kobe collection. *Int. J. Climatol.*, **25**, 865–879, <https://doi.org/10.1002/joc.1169>.
- Iyer, S., and K. Drushka, 2021a: The influence of preexisting stratification and tropical rain modes on the mixed layer salinity response to rainfall. *J. Geophys. Res. Oceans*, **126**, e2021JC017574, <https://doi.org/10.1029/2021JC017574>.
- , and —, 2021b: Turbulence within rain-formed fresh lenses during the SPURS-2 experiment. *J. Phys. Oceanogr.*, **51**, 1705–1721, <https://doi.org/10.1175/JPO-D-20-0303.1>.
- Jin, D., L. Oreopoulos, D. Lee, N. Cho, and J. Tan, 2018: Contrasting the co-variability of daytime cloud and precipitation over tropical land and ocean. *Atmos. Chem. Phys.*, **18**, 3065–3082, <https://doi.org/10.5194/acp-18-3065-2018>.
- Johnson, G. C., B. M. Sloyan, W. S. Kessler, and K. E. McTaggart, 2002: Direct measurements of upper ocean currents and water properties across the tropical Pacific during the 1990s. *Prog. Oceanogr.*, **52**, 31–61, [https://doi.org/10.1016/S0079-6611\(02\)00021-6](https://doi.org/10.1016/S0079-6611(02)00021-6).
- Kato, H., and O. Phillips, 1969: On the penetration of a turbulent layer into stratified fluid. *J. Fluid Mech.*, **37**, 643–655, <https://doi.org/10.1017/S0022112069000784>.
- Large, W. G., and S. Yeager, 2009: The global climatology of an interannually varying air–sea flux data set. *Climate Dyn.*, **33**, 341–364, <https://doi.org/10.1007/s00382-008-0441-3>.
- , J. C. McWilliams, and S. C. Doney, 1994: Oceanic vertical mixing: A review and a model with a nonlocal boundary layer parameterization. *Rev. Geophys.*, **32**, 363–403, <https://doi.org/10.1029/94RG01872>.
- Laxague, N. J., and C. J. Zappa, 2020: The impact of rain on ocean surface waves and currents. *Geophys. Res. Lett.*, **47**, e2020GL087287, <https://doi.org/10.1029/2020GL087287>.
- Lien, R.-C., D. R. Caldwell, M. Gregg, and J. N. Moum, 1995: Turbulence variability at the equator in the central Pacific at the beginning of the 1991–1993 El Niño. *J. Geophys. Res.*, **100**, 6881–6898, <https://doi.org/10.1029/94JC03312>.
- Masich, J., W. S. Kessler, M. F. Cronin, and K. R. Grissom, 2021: Diurnal cycles of near-surface currents across the tropical Pacific. *J. Geophys. Res. Oceans*, **126**, e2020JC016982, <https://doi.org/10.1029/2020JC016982>.
- Masunaga, H., T. S. L'Ecuyer, and C. D. Kummerow, 2005: Variability in the characteristics of precipitation systems in the tropical Pacific. Part I: Spatial structure. *J. Climate*, **18**, 823–840, <https://doi.org/10.1175/JCLI-3304.1>.
- McPhaden, M. J., and Coauthors, 2010: The Global Tropical Moored Buoy Array. *Proc. OceanObs*, **9**, 668–682, <https://doi.org/10.5270/OceanObs09.cwp.61>.
- Meehl, G., P. Gent, J. Arblaster, B. Otto-Bliesner, E. Brady, and A. Craig, 2001: Factors that affect the amplitude of El Niño in global coupled climate models. *Climate Dyn.*, **17**, 515–526, <https://doi.org/10.1007/PL00007929>.
- Monin, A. S., and A. M. Obukhov, 1954: Basic laws of turbulent mixing in the surface layer of the atmosphere. *Tr. Geofiz. Inst., Akad. Nauk SSSR*, **24**, 163–187.
- Moum, J. N., 2021: Variations in ocean mixing from seconds to years. *Annu. Rev. Mar. Sci.*, **13**, 201–226, <https://doi.org/10.1146/annurev-marine-031920-122846>.
- , and J. Nash, 2009: Mixing measurements on an equatorial ocean mooring. *J. Atmos. Oceanic Technol.*, **26**, 317–336, <https://doi.org/10.1175/2008JTECHO617.1>.
- , D. R. Caldwell, and C. A. Paulson, 1989: Mixing in the equatorial surface layer and thermocline. *J. Geophys. Res.*, **94**, 2005–2022, <https://doi.org/10.1029/JC094iC02p02005>.
- , R.-C. Lien, A. Perlin, J. Nash, M. Gregg, and P. Wiles, 2009: Sea surface cooling at the equator by subsurface mixing in tropical instability waves. *Nat. Geosci.*, **2**, 761–765, <https://doi.org/10.1038/ngeo657>.
- , A. Perlin, J. D. Nash, and M. J. McPhaden, 2013: Seasonal sea surface cooling in the equatorial Pacific cold tongue controlled by ocean mixing. *Nature*, **500**, 64–67, <https://doi.org/10.1038/nature12363>.
- Osborn, T., 1980: Estimates of the local rate of vertical diffusion from dissipation measurements. *J. Phys. Oceanogr.*, **10**, 83–89, [https://doi.org/10.1175/1520-0485\(1980\)010<0083:EOTLRO>2.0.CO;2](https://doi.org/10.1175/1520-0485(1980)010<0083:EOTLRO>2.0.CO;2).
- Pacanowski, R., and S. Philander, 1981: Parameterization of vertical mixing in numerical models of tropical oceans. *J. Phys. Oceanogr.*, **11**, 1443–1451, [https://doi.org/10.1175/1520-0485\(1981\)011<1443:POVMIN>2.0.CO;2](https://doi.org/10.1175/1520-0485(1981)011<1443:POVMIN>2.0.CO;2).
- Pei, S., T. Shinoda, W. Wang, and R.-C. Lien, 2020: Simulation of deep cycle turbulence by a global ocean general circulation model. *Geophys. Res. Lett.*, **47**, e2020GL088384, <https://doi.org/10.1029/2020GL088384>.
- Pendergrass, A. G., 2018: What precipitation is extreme? *Science*, **360**, 1072–1073, <https://doi.org/10.1126/science.aat1871>.
- Perlin, A., and J. Moum, 2012: Comparison of thermal variance dissipation rates from moored and profiling instruments at the equator. *J. Atmos. Oceanic Technol.*, **29**, 1347–1362, <https://doi.org/10.1175/JTECH-D-12-00019.1>.
- Peters, H., M. Gregg, and J. Toole, 1988: On the parameterization of equatorial turbulence. *J. Geophys. Res.*, **93**, 1199–1218, <https://doi.org/10.1029/JC093iC02p01199>.
- Pham, H. T., and S. Sarkar, 2017: Turbulent entrainment in a strongly stratified barrier layer. *J. Geophys. Res. Oceans*, **122**, 5075–5087, <https://doi.org/10.1002/2016JC012357>.
- , W. D. Smyth, S. Sarkar, and J. N. Moum, 2017: Seasonality of deep cycle turbulence in the eastern equatorial Pacific. *J. Phys. Oceanogr.*, **47**, 2189–2209, <https://doi.org/10.1175/JPO-D-17-0008.1>.
- Pollard, R. T., P. B. Rhines, and R. O. Thompson, 1973: The deepening of the wind-mixed layer. *Geophys. Fluid Dyn.*, **4**, 381–404, <https://doi.org/10.1080/03091927208236105>.
- Price, J. F., 1979: Observations of a rain-formed mixed layer. *J. Phys. Oceanogr.*, **9**, 643–649, [https://doi.org/10.1175/1520-0485\(1979\)009<0643:OARFM>2.0.CO;2](https://doi.org/10.1175/1520-0485(1979)009<0643:OARFM>2.0.CO;2).
- Qiao, L., and R. H. Weisberg, 1997: The zonal momentum balance of the equatorial undercurrent in the central Pacific. *J. Phys. Oceanogr.*, **27**, 1094–1119, [https://doi.org/10.1175/1520-0485\(1997\)027<1094:TZMBOT>2.0.CO;2](https://doi.org/10.1175/1520-0485(1997)027<1094:TZMBOT>2.0.CO;2).
- Richards, K. J., S.-P. Xie, and T. Miyama, 2009: Vertical mixing in the ocean and its impact on the coupled ocean–atmosphere system in the eastern tropical Pacific. *J. Climate*, **22**, 3703–3719, <https://doi.org/10.1175/2009JCLI2702.1>.
- Rickenbach, T. M., and S. A. Rutledge, 1998: Convection in TOGA COARE: Horizontal scale, morphology, and rainfall production. *J. Atmos. Sci.*, **55**, 2715–2729, [https://doi.org/10.1175/1520-0469\(1998\)055<2715:CITCHS>2.0.CO;2](https://doi.org/10.1175/1520-0469(1998)055<2715:CITCHS>2.0.CO;2).
- Ropelewski, C. F., and M. S. Halpert, 1987: Global and regional scale precipitation patterns associated with the El Niño/Southern Oscillation. *Mon. Wea. Rev.*, **115**, 1606–1626, [https://doi.org/10.1175/1520-0493\(1987\)115<1606:GARSPP>2.0.CO;2](https://doi.org/10.1175/1520-0493(1987)115<1606:GARSPP>2.0.CO;2).
- , and —, 1996: Quantifying southern oscillation-precipitation relationships. *J. Climate*, **9**, 1043–1059, [https://doi.org/10.1175/1520-0442\(1996\)009<1043:QSOPR>2.0.CO;2](https://doi.org/10.1175/1520-0442(1996)009<1043:QSOPR>2.0.CO;2).

- Schlüssel, P., A. V. Soloviev, and W. J. Emery, 1997: Cool and freshwater skin of the ocean during rainfall. *Bound.-Layer Meteor.*, **82**, 439–474, <https://doi.org/10.1023/A:1000225700380>.
- Schudlich, R. R., and J. F. Price, 1992: Diurnal cycles of current, temperature, and turbulent dissipation in a model of the equatorial upper ocean. *J. Geophys. Res.*, **97**, 5409–5422, <https://doi.org/10.1029/91JC01918>.
- Shchepetkin, A. F., and J. C. McWilliams, 2005: The Regional Oceanic Modeling System (ROMS): A split-explicit, free-surface, topography-following-coordinate oceanic model. *Ocean Modell.*, **9**, 347–404, <https://doi.org/10.1016/j.oceanmod.2004.08.002>.
- Shcherbina, A. Y., E. A. D’Asaro, and R. R. Harcourt, 2019: Rain and sun create slippery layers in eastern Pacific fresh pool. *Oceanography*, **32**, 98–107, <https://doi.org/10.5670/oceanog.2019.217>.
- Smyth, W., and J. Moum, 2013: Marginal instability and deep cycle turbulence in the eastern equatorial Pacific Ocean. *Geophys. Res. Lett.*, **40**, 6181–6185, <https://doi.org/10.1002/2013GL058403>.
- , P. Zavialov, and J. Moum, 1997: Decay of turbulence in the upper ocean following sudden isolation from surface forcing. *J. Phys. Oceanogr.*, **27**, 810–822, [https://doi.org/10.1175/1520-0485\(1997\)027<0810:DOTITU>2.0.CO;2](https://doi.org/10.1175/1520-0485(1997)027<0810:DOTITU>2.0.CO;2).
- , J. Moum, L. Li, and S. Thorpe, 2013: Diurnal shear instability, the descent of the surface shear layer, and the deep cycle of equatorial turbulence. *J. Phys. Oceanogr.*, **43**, 2432–2455, <https://doi.org/10.1175/JPO-D-13-089.1>.
- , H. Pham, J. Moum, and S. Sarkar, 2017: Pulsating turbulence in a marginally unstable stratified shear flow. *J. Fluid Mech.*, **822**, 327–341, <https://doi.org/10.1017/jfm.2017.283>.
- , S. Warner, J. Moum, H. Pham, and S. Sarkar, 2021: What controls the deep cycle? Proxies for equatorial turbulence. *J. Phys. Oceanogr.*, **51**, 2291–2302, <https://doi.org/10.1175/JPO-D-20-0236.1>.
- Stephens, G., M. Smalley, and M. Lebsock, 2019: The cloudy nature of tropical rains. *J. Geophys. Res.*, **124**, 171–188, <https://doi.org/10.1029/2018JD029394>.
- Sutherland, G., L. Marié, G. Reverdin, K. H. Christensen, G. Broström, and B. Ward, 2016: Enhanced turbulence associated with the diurnal jet in the ocean surface boundary layer. *J. Phys. Oceanogr.*, **46**, 3051–3067, <https://doi.org/10.1175/JPO-D-15-0172.1>.
- Taylor, J. R., 2008: Numerical simulations of the stratified oceanic bottom boundary layer. Ph.D. thesis, University of California, San Diego, 231 pp.
- ten Doeschate, A., G. Sutherland, H. Bellenger, S. Landwehr, L. Esters, and B. Ward, 2019: Upper ocean response to rain observed from a vertical profiler. *J. Geophys. Res. Oceans*, **124**, 3664–3681, <https://doi.org/10.1029/2018JC014060>.
- Thompson, E. J., J. N. Moum, C. W. Fairall, and S. A. Rutledge, 2019: Wind limits on rain layers and diurnal warm layers. *J. Geophys. Res. Oceans*, **124**, 897–924, <https://doi.org/10.1029/2018JC014130>.
- Tokay, A., D. A. Short, C. R. Williams, W. L. Ecklund, and K. S. Gage, 1999: Tropical rainfall associated with convective and stratiform clouds: Intercomparison of disdrometer and profiler measurements. *J. Appl. Meteor.*, **38**, 302–320, [https://doi.org/10.1175/1520-0450\(1999\)038<0302:TRAWCA>2.0.CO;2](https://doi.org/10.1175/1520-0450(1999)038<0302:TRAWCA>2.0.CO;2).
- Trenberth, K. E., and J. M. Caron, 2000: The southern oscillation revisited: Sea level pressures, surface temperatures, and precipitation. *J. Climate*, **13**, 4358–4365, [https://doi.org/10.1175/1520-0442\(2000\)013<4358:TSORSLS>2.0.CO;2](https://doi.org/10.1175/1520-0442(2000)013<4358:TSORSLS>2.0.CO;2).
- Trowbridge, J., 1992: A simple description of the deepening and structure of a stably stratified flow driven by a surface stress. *J. Geophys. Res.*, **97**, 15 529–15 543, <https://doi.org/10.1029/92JC01512>.
- Tsujino, H., and Coauthors, 2018: JRA-55 based surface dataset for driving ocean–sea-ice models (JRA55-do). *Ocean Modell.*, **130**, 79–139, <https://doi.org/10.1016/j.oceanmod.2018.07.002>.
- Walesby, K., J. Vialard, P. J. Minnett, A. H. Callaghan, and B. Ward, 2015: Observations indicative of rain-induced double diffusion in the ocean surface boundary layer. *Geophys. Res. Lett.*, **42**, 3963–3972, <https://doi.org/10.1002/2015GL063506>.
- Wang, W., and M. J. McPhaden, 1999: The surface-layer heat balance in the equatorial Pacific Ocean. Part I: Mean seasonal cycle. *J. Phys. Oceanogr.*, **29**, 1812–1831, [https://doi.org/10.1175/1520-0485\(1999\)029<1812:TSLHBI>2.0.CO;2](https://doi.org/10.1175/1520-0485(1999)029<1812:TSLHBI>2.0.CO;2).
- Warner, S. J., and J. N. Moum, 2019: Feedback of mixing to ENSO phase change. *Geophys. Res. Lett.*, **46**, 13 920–13 927, <https://doi.org/10.1029/2019GL085415>.
- Whitt, D., 2022a: Analysis and visualization software for “rain impacts on the surface atmosphere and upper ocean in the central equatorial Pacific.” Zenodo, <https://doi.org/10.5281/zenodo.5907020>.
- , 2022b: DIABLO LES software and configuration file update for TPOS array: 28 simulations along the equator from 165°W to 100°W. Zenodo, <http://doi.org/10.5281/zenodo.5904362>.
- , 2022c: Online data for “rain impacts on the surface atmosphere and upper ocean in the central equatorial Pacific.” Figshare, <https://doi.org/10.6084/m9.figshare.19068164>.
- , 2022d: Addendum to online data for “rain impacts on the surface atmosphere and upper ocean in the central equatorial Pacific.” Figshare, <https://doi.org/10.6084/m9.figshare.19699711>.
- , S. Nicholson, and M. Carranza, 2019: Global impacts of sub-seasonal (<60 day) wind variability on ocean surface stress, buoyancy flux, and mixed layer depth. *J. Geophys. Res. Oceans*, **124**, 8798–8831, <https://doi.org/10.1029/2019JC015166>.
- , D. Cherian, R. Holmes, S. Bachman, R. Lien, W. Large, and J. Moum, 2022: Simulation and scaling of the turbulent vertical heat transport and deep-cycle turbulence across the equatorial Pacific cold tongue. *J. Phys. Oceanogr.*, **52**, 981–1014, <https://doi.org/10.1175/JPO-D-21-0153.1>.
- Wijesekera, H. W., and M. C. Gregg, 1996: Surface layer response to weak winds, westerly bursts, and rain squalls in the western Pacific warm pool. *J. Geophys. Res.*, **101**, 977–997, <https://doi.org/10.1029/95JC02553>.
- , C. Paulson, and A. Huyer, 1999: The effect of rainfall on the surface layer during a westerly wind burst in the western equatorial Pacific. *J. Phys. Oceanogr.*, **29**, 612–632, [https://doi.org/10.1175/1520-0485\(1999\)029<0612:TEOROT>2.0.CO;2](https://doi.org/10.1175/1520-0485(1999)029<0612:TEOROT>2.0.CO;2).
- Young, I., 1999: Seasonal variability of the global ocean wind and wave climate. *Int. J. Climatol.*, **19**, 931–950, [https://doi.org/10.1002/\(SICI\)1097-0088\(199907\)19:9<931::AID-JOC412>3.0.CO;2-O](https://doi.org/10.1002/(SICI)1097-0088(199907)19:9<931::AID-JOC412>3.0.CO;2-O).
- Zappa, C. J., D. T. Ho, W. R. McGillis, M. L. Banner, J. W. Dacey, L. F. Bliven, B. Ma, and J. Nystuen, 2009: Rain-induced turbulence and air-sea gas transfer. *J. Geophys. Res.*, **114**, C07009, <https://doi.org/10.1029/2008JC005008>.
- Zaron, E. D., and J. N. Moum, 2009: A new look at Richardson number mixing schemes for equatorial ocean modeling. *J. Phys. Oceanogr.*, **39**, 2652–2664, <https://doi.org/10.1175/2009JPO4133.1>.
- Zhu, Y., and R.-H. Zhang, 2019: A modified vertical mixing parameterization for its improved ocean and coupled simulations in the tropical Pacific. *J. Phys. Oceanogr.*, **49**, 21–37, <https://doi.org/10.1175/JPO-D-18-0100.1>.